

# 1 Neutron-Neutron Correlations in the Photofission of U-238

2 J. Burggraf, D.S. Dale, and T. Forest  
3

4      *Department of Physics,*  
5      *Idaho State University, Pocatello, ID 83201*

6 G. Warren, S. Stave, S. Behling, and E. Church  
7

8      *Pacific Northwest National Laboratory, PO Box 999, Richland, Washington 99352*

(Dated: October 15, 2019)

9 **Background:** In the fission of actinides, the nearly back-to-back motion of the fission fragments has a strong  
10 effect on the kinematics of fission neutrons. This leads to a favoring of opening angles near  $0^\circ$  and  $180^\circ$  in the  
11 neutron-neutron (n-n) opening angle distribution of correlated neutron pairs from the same fission event.

12 **Purpose:** To measure the n-n opening angle and energy correlations in the photofission of  $^{238}\text{U}$ . As of this  
13 writing, measurements of correlated n-n opening angle distributions have been reported only for the spontaneous  
14 and neutron-induced fission of actinides. This work is the first to report such a measurement using photofission  
15 and will provide useful experimental input for photofission models used in codes such as MCNP and FREYA.

16 **Method:** Fission is induced using bremsstrahlung photons produced via a low duty factor, pulsed, linear electron  
17 accelerator. The bremsstrahlung photon beam impinges upon a  $^{238}\text{U}$  target that is surrounded by a large neutron  
18 scintillation detection system capable of measuring particle position and time of flight, from which n-n opening  
19 angle and energy are measured. Neutron-neutron angular correlations are determined by taking the ratio between  
20 a correlated n-n distribution and an uncorrelated n-n distribution formed by the pairing of neutrons produced  
21 during different beam pulses. This analysis technique greatly diminishes effects due to detector efficiencies,  
22 acceptance, and experimental drifts.

23 **Results:** The angular correlation of neutrons from the photofission of  $^{238}\text{U}$  shows a high dependence on neutron  
24 energy as well as a dependence on the angle of the emitted neutrons with respect to the incoming photon beam.  
25 Angular correlations were also measured using neutrons from the spontaneous fission of  $^{252}\text{Cf}$ , showing good  
26 agreement with past measurements.

27 **Conclusions:** The measured angular correlations reflect the underlying back-to-back nature of the fission fragments.  
28 An anomalous decline in n-n yield was observed for opening angles near  $180^\circ$  for  $^{238}\text{U}$ .

## 29 CONTENTS

30 I. Overview of Neutron-Neutron Angular  
31 Correlations in Fission  
32    A. Theoretical Basis  
33    B. Past Measurements: Spontaneous and  
34       Neutron Induced Fission  
35    C. Considerations for Photofission

36 II. Experimental Setup  
37    A. Detectors  
38    B. Detector Shielding  
39    C. Bremsstrahlung Photon Beam  
40    D. DU Target  
41    E. Electronics

42 III. Measurement Techniques  
43    A. Particle Time of Flight and Energy  
44       Determination  
45    B. Particle Position Reconstruction  
46    C. Measurements with  $^{252}\text{Cf}$

47 IV. Analysis  
48    A. Cancelation of Detector Efficiencies, Drifts,  
49       and Geometric Phase Space  
50    B. Subtraction of Accidental Coincidences

## 51 V. Potential sources of error

52    A. Correlated versus uncorrelated n-n energy  
53       distribution  
54    B. Detector Cross-talk  
55       1. Simulation of Detector Cross-talk  
56       C. Neutron Scattering within the Target

## 57 VI. Results

58    A. Comparisons with FREYA  
59    B. Anomalous emission at large opening  
60       angles  
61       C. Considering  $\theta_{abs}$

## 62 VII. Concluding Remarks

## 63 VIII. Acknowledgments

## 64 References

## 65 I. OVERVIEW OF NEUTRON-NEUTRON 66 ANGULAR CORRELATIONS IN FISSION

67 The fission process is characterized by the emission of  
68 neutrons. The time taken for a neutron to be emitted can  
69 be categorized as either prompt or delayed. Prompt

70 fission neutrons are defined as neutrons that are emitted either immediately after ( $< 10^{-14}$  seconds) fission,  
 71 or during the scission of the nucleus, and account for  
 72  $\sim 99\%$  of neutron emission [1]. Delayed neutrons are not  
 73 relevant to the present work because they account for  
 74 only  $\sim 1\%$  of total neutron emission in actinide photofission [1], and they are emitted milliseconds to minutes  
 75 after fission which is well outside the neutron acceptance  
 76 timing window of the present work.

77 Prompt fission neutron production occurs by means of  
 78 two distinct mechanisms. The dominant mechanism is  
 79 neutron emission from the fully accelerated fragments.  
 80 The second mechanism, referred to as *early* or *scission*  
 81 neutron emission, is the emission of neutrons during ei-  
 82 ther the scission of the nucleus or the acceleration of the  
 83 fission fragments. A large number of past studies have  
 84 established that the majority of prompt fission neutrons  
 85 (80%–98%) are emitted from the fully accelerated frag-  
 86 ments, while scission neutrons account for the remaining  
 87 2%–20% percent [2]. The nature of scission neutrons has  
 88 remained elusive since their first tentative observation in  
 89 1962 by Bowman *et al.* [3].

### 92 A. Theoretical Basis

93 The neutron-neutron (n-n) opening angle distribution  
 94 of correlated neutron pairs, as seen in the lab frame, is  
 95 widely used for the quantification of n-n angular correla-  
 96 tions. Angular correlations in fission neutrons arise due  
 97 to the kinematics of the fission fragments. It has been  
 98 shown that neutrons released from the fully accelerated  
 99 fission fragments are evaporated isotropically in the frag-  
 100 ment’s rest frame, and are emitted at speeds compara-  
 101 ble to that of the fragments themselves [4]. This leads  
 102 to the well-known U-shaped distribution in neutron-  
 103 neutron opening angle ( $\theta_{nn}$ ), which has been reported  
 104 in studies of neutron-induced, spontaneous, and in this  
 105 work, photofission.

106 The U-shaped distribution of  $\theta_{nn}$  can be understood  
 107 as the result of the boost provided to the neutrons by the  
 108 fission fragments in binary fission. Due to the conserva-  
 109 tion of momentum, the fully accelerated fission fragments  
 110 are traveling nearly back-to-back, and neutrons emitted  
 111 from different fragments are boosted in opposite direc-  
 112 tions, whereas neutrons emitted from the same fragment  
 113 are boosted in the same direction. Thus, because the  
 114 velocities of the fission fragments are large enough to ac-  
 115 count for a significant portion of the kinetic energy of  
 116 fission neutrons, neutron pairs emitted from the acceler-  
 117 ated fragments exhibit a favoring of opening angles near  
 118 0° if emitted from the same fragment and 180° if emit-  
 119 ted from different fragments, and consequently, result in  
 120 a suppression of opening angles near 90°.

121 The favoring of large and small n-n opening angles  
 122 shows a strong dependence on neutron energy. Neutrons  
 123 with higher energy are more likely to have been emit-  
 124 ted along the same direction as the fission fragments and

125 are therefore expected to favor large and small opening  
 126 angles. On the other hand, neutrons emitted with lower  
 127 energy are more susceptible to kinematical focusing along  
 128 the direction of the recoil of the emitting fragment. The  
 129  $\theta_{nn}$  distribution and its dependence on neutron energy  
 130 are expected to shed light on several fundamental aspects  
 131 of the fission process including the neutron multiplicity  
 132 distributions associated with the light and heavy fission  
 133 fragments, the nuclear temperatures of the fission frag-  
 134 ments, and the mass distribution of the fission fragments  
 135 as a function of energy released. In addition, the unique  
 136 kinematics of fission and the resulting n-n correlations  
 137 have the potential to be the basis for a new tool to char-  
 138 acterize fissionable materials [5].

### 139 B. Past Measurements: Spontaneous and Neutron 140 Induced Fission

141 The first measurement of the angular correlation  
 142 among coincident neutrons from fission was performed  
 143 by Debenedetti *et al.* [6] in 1948 from neutron induced  
 144 fission of  $^{235}\text{U}$ . The next measurement of this type was  
 145 performed by Pringle and Brooks in 1975 [7], in which  
 146 neutrons emitted from the spontaneous fission (SF) of  
 147  $^{252}\text{Cf}$  were found to have high coincidence rates at small  
 148 opening angles near 0° and large opening angles near  
 149 180°. In order to produce a result that is insensitive to  
 150 the effects of detector geometry and efficiency, the present  
 151 work uses techniques similar to those used in reference [7],  
 152 in which a ratio is taken between a correlated opening an-  
 153 gle distribution and an uncorrelated opening angle distri-  
 154 bution. Measurements of n-n angular correlation in the  
 155 SF of  $^{252}\text{Cf}$ , the most studied case of correlated neutron  
 156 emission in fission (see Refs. [7–10]), were also performed  
 157 in the present work and show good agreement with past  
 158 measurements, as seen in Fig. 1. Correlated n-n measure-  
 159 ments have also been performed using thermal neutron  
 160 induced fission of  $^{235}\text{U}$ ,  $^{233}\text{U}$ , and  $^{239}\text{Pu}$  [11], as well as  
 161 the SF of  $^{240}\text{Pu}$  [12].

### 163 C. Considerations for Photofission

164 The photofission reaction occurs during the de-  
 165 excitation of a nucleus after the absorption of a pho-  
 166 ton. For photon energies between 6 and 25 MeV, this  
 167 absorption occurs primarily via the giant dipole reso-  
 168 nance (GDR) excitation. One distinct and useful as-  
 169 pect of photofission, relative to neutron-induced fission,  
 170 is the low transfer of angular momentum to the nucleus,  
 171 which gives rise to a simpler set of selection rules for  
 172 the transfer of angular momentum. For the photofis-  
 173 sion of even-even nuclei, excitation occurs primarily via  
 174 electric dipole transitions, and to a lesser extent electric  
 175 quadrupole transitions, which gives rise to anisotropies  
 176 in the fission fragment angular distributions that are far  
 177 more pronounced than for other types of fission [13, 14].

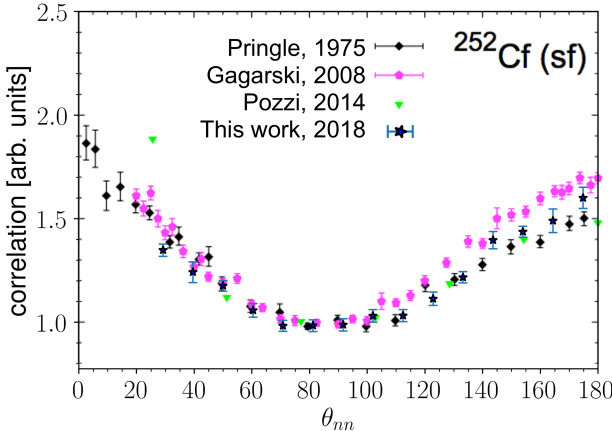


**FIG. 1:**  $\theta_{nn}$  distribution from the spontaneous fission of  $^{252}\text{Cf}$ . The minimum neutron energy cut-off for Pringle [7], Gagarski [9], and Pozzi [12] is 0.425 MeV, 0.425 MeV, and 0.7 MeV, respectively, and for this work is 0.4 MeV.

These anisotropies are expressed in the angular distribution of emitted neutrons. For these reasons, photofission is increasingly being used as a means to study sub-nuclear structures and the fundamentals of the fission process. Such studies are needed in order to validate various model parameters required for an accurate theoretical description of the fission process.

## II. EXPERIMENTAL SETUP

This experiment was carried out at the Idaho Accelerator Center (IAC), using their short-pulsed linear accelerator, which is an L-band frequency (1300 MHz) electron linear accelerator. See section II C for the accelerator parameters used during the experiment. Figure 2 shows a top-down diagram of the experimental arrangement.

### A. Detectors

The detection system measures neutron position and time of flight (ToF), which is defined as the time taken for a particle to travel from the fission target to a detector. The purpose of the ToF measurement is to determine the kinetic energy of detected neutrons and to distinguish between photons and neutrons. The detection system's positional precision is  $\pm 9$  cm, which results in an average opening angular precision of  $\pm 6^\circ$  for a target to detector distance of 1.25 m. The detection system consists of fourteen shielded scintillators made from Polyvinyl Toluene (PVT) arranged in a ring around the target (see Figs. 2 and 3). Attached to both ends of each scintillator are 10-cm long, non-scintillating, ultra-violet transmitting, plastic light-guides. A Hamamatsu 580-17 photomultiplier (PMT) tube is fixed to each light-guide using optical glue. In order to increase the chance that

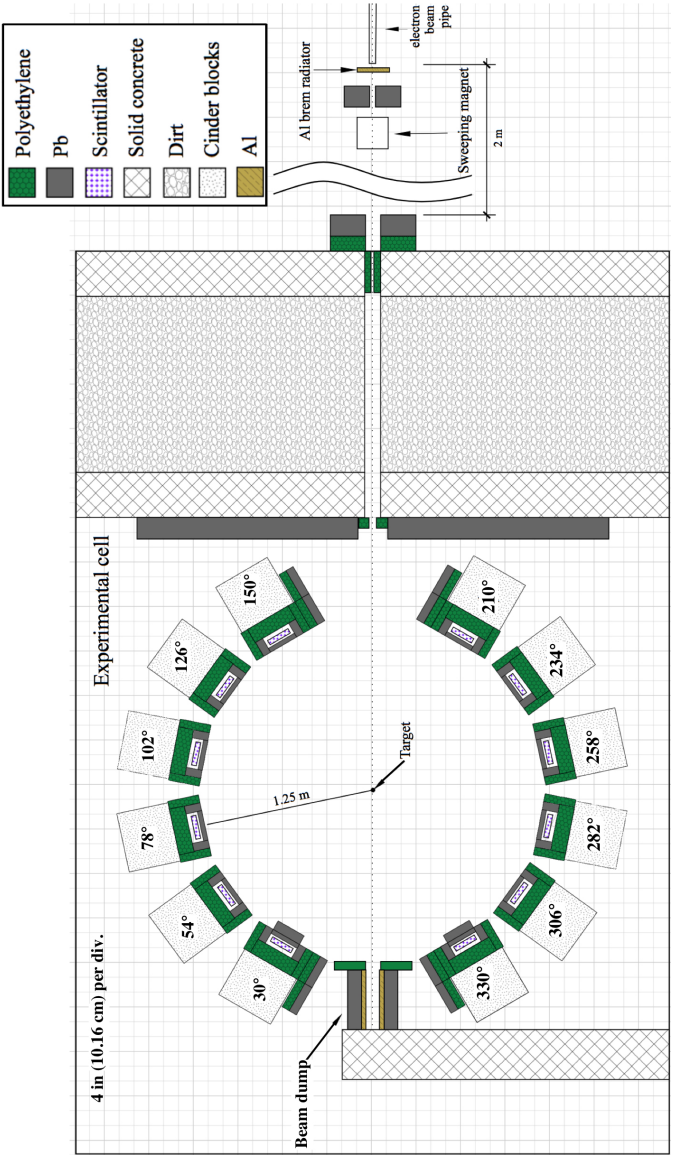


**FIG. 2:** To-scale, top down diagram of the experimental setup. An electron beam impinges upon a 3.8 cm thick Al radiator, and the resulting bremsstrahlung beam enters the experimental cell from the top of the figure. The supporting structure for each detector has been labeled according to the angle, in degrees, between the center of each detector and direction of the incoming photon beam. The fission target, a  $0.05 \times 2 \times 4 \text{ cm}^3$   $^{238}\text{U}$  cuboid, is rotated slowly about the vertical axis in order to mimic the effect of using a cylindrical target.

scintillation light remains inside the scintillator, the scintillators were polished to remove micro-imperfections and were then wrapped in reflective aluminized mylar.

Ten of the fourteen scintillators had dimensions of  $76.2 \times 15.2 \times 3.8 \text{ cm}^3$ . The remaining four, located the nearest to the beam line at  $\pm 30^\circ$  with respect to the beam, had dimensions of  $25.4 \times 15.2 \times 3.8 \text{ cm}^3$ . These scintillators, 1/3 the length of the rest, are the result of the

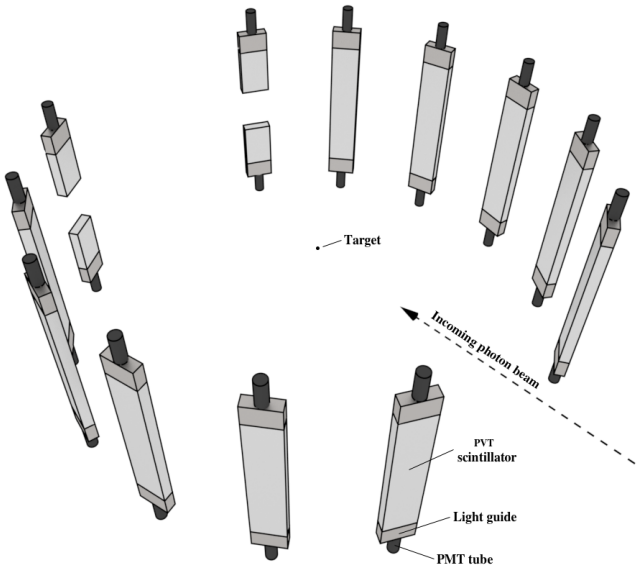


**FIG. 3:** 3-D rendering of the bare, unshielded scintillators, along with PMTs and light guides. Most of the open space between the scintillators was occupied by shielding, as seen in Fig. 2.

218 segmentation of two normally sized scintillators in order  
219 to lower the relatively high photon detection rates near  
220 the beam line. Prior to segmentation, a photon was reg-  
221 istered in the forward-most detectors at a rate of about  
222 0.9 photons per pulse, and because the electronics were  
223 operated in single hit mode (see section II E), this greatly  
224 reduced the effective neutron detection efficiency. After  
225 segmentation and optimization of shielding, the photon  
226 detection rate was about 0.2 photons per pulse in each  
227 segmented detector. The segmented detectors also differ  
228 from the rest in that they were instrumented with only a  
229 single PMT, and therefore provide a comparatively lower  
230 precision in energy and position measurements. In order  
231 to test for systematic errors that may have resulted from  
232 the use of the segmented detectors, opening angle mea-  
233 surements were compared with and without their use,  
234 and the differences were well within experimental errors.  
235

The relative efficiencies of the neutron detectors as a  
236 function of neutron energy and detector location were  
237 calculated by dividing the measured by the yields of neu-  
238 trons from the SF of  $^{252}\text{Cf}$  according to MCNP. The re-  
239 sults are shown in Fig. 4. Note that the effects of the  
240 uncertainty in measured neutron energy (seen in Fig. 10)  
241 are folded into this calculation. The analysis techniques  
242 described in section IV are designed to eliminate the ef-  
243 fects of detector efficiency from the final result.

245

## B. Detector Shielding

246 The detector shielding, depicted in Fig. 5, was con-  
247 structed using lead and polyethylene with the aim of re-  
248 ducing detector cross-talk, the detection of photons, and

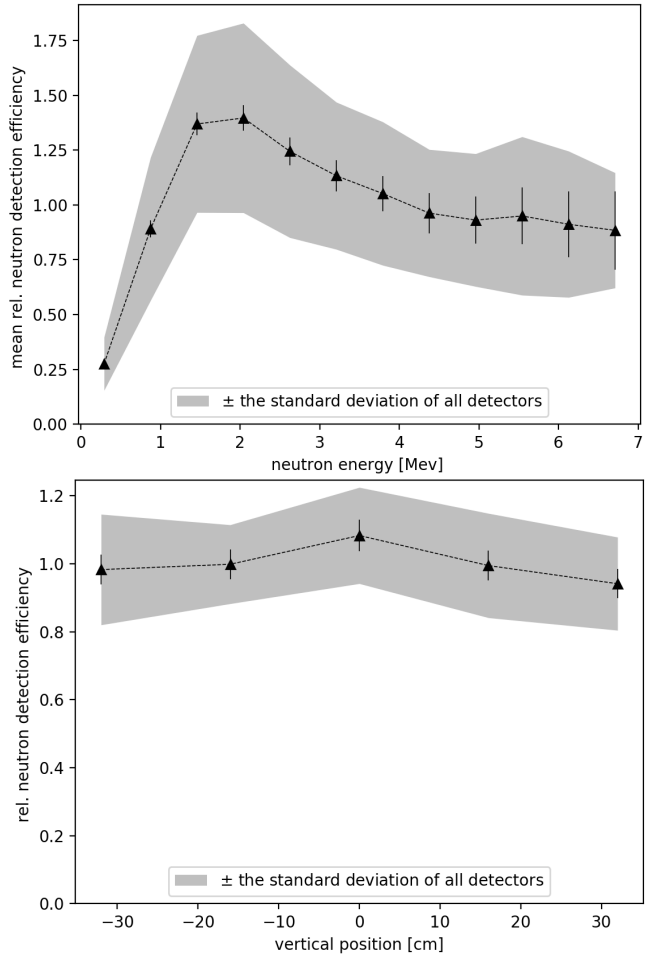


**FIG. 4:** (top) The mean relative neutron detection efficiency of all detectors as a function of neutron energy is calculated by dividing the measured energy distribution by the known energy distribution of neutrons from the SF of  $^{252}\text{Cf}$ . The relative efficiency differs from detector to detector, as demonstrated by the shaded region, which corresponds to the standard deviation of the relative efficiencies of all detectors. The error bars represent the uncertainty in the mean. (bot) Mean relative neutron detection efficiency as a function of the reconstructed position along the detectors longest axis.

249 noise. The sides of each scintillator were shielded with  
250 5 cm of lead followed by 5 cm of polyethylene to reduce  
251 the chance of neutron cross-talk. Lead was not placed  
252 behind the scintillators after an MCNP-POLIMI simula-  
253 tion indicated that the additional lead would significantly  
254 increase cross-talk rates. Instead, 10 cm of polyethylene  
255 was placed behind the scintillators. For a detailed dis-  
256 cussion about the issue of cross-talk, see section V B.

257 The front face of each detector was subject to  
258 the highest photon flux due to the scattering of the  
259 bremsstrahlung beam from the target. The detection of  
260 a photon renders the given detector unable to detect any  
261 subsequent fission neutrons from the same pulse due to  
262 the detector recovery time. Lead mitigates this prob-

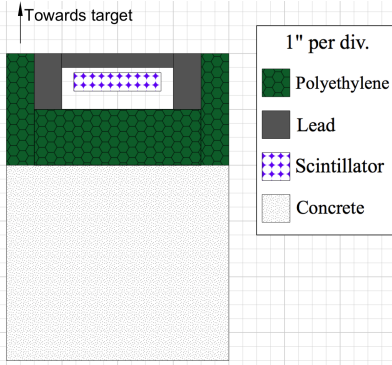


**FIG. 5:** Detector shielding was designed to reduce the detection of photons, room return, and detector cross-talk.

263 lem by reducing photon flux, but has the side effect of  
 264 scattering neutrons. If a neutron scatters prior to being  
 265 detected, the ToF measurement and position reconstruc-  
 266 tion are corrupted. The extent of measurement errors  
 267 caused by lead shielding were quantified using an MCNP  
 268 simulation, and, accordingly, 2.5 cm of lead was placed  
 269 along the front face of the detectors. This diminished  
 270 photon detection rates to reasonable levels, and, accord-  
 271 ing to the simulation, leads to a root-mean-square error  
 272 in opening angle and ToF of  $1^\circ$  and 0.3 ns, respectively,  
 273 due to neutron elastic scattering.

274 Because of the particularly high photon flux at the  
 275 sides of all detectors located directly adjacent to the  
 276 beam, an additional 2" of lead was placed along the sides  
 277 of these detectors. For the same reason, an additional 2"  
 278 of lead was also placed along the front faces of the de-  
 279 tectors farthest downstream, located at  $\pm 30^\circ$  from the  
 280 beam line. The differences in shielding design among the  
 281 detectors can be seen in Fig. 2.

303

### C. Bremsstrahlung Photon Beam

284 In order to ensure that all correlated neutrons pro-  
 285 duced are due to fission, the bremsstrahlung end-point  
 286 energy was set to 10.5 MeV, safely below the  $(\gamma, 2n)$   
 287 threshold of 11.28 MeV for  $^{238}\text{U}$ . Aluminum was chosen  
 288 for the bremsstrahlung radiator because it has a neu-  
 289 tron knockout threshold above the energy of the elec-  
 290 tron beam, which ensured that the radiator would not  
 291 be a source of fast neutrons with the potential to in-  
 292 terfere with the experiment. A sweeping magnet was  
 293 placed downstream from the bremsstrahlung radiator to  
 294 remove charged particles from the photon beam. Fol-  
 295 lowing the sweeping magnet, the beam traveled through  
 296 a series of polyethylene and lead collimators on its way  
 297 into the experimental cell in which the target was located  
 298 (see Fig. 2). Figure 6 shows the energy distribution of  
 299 photons that reach the target according to an MCNP  
 300 simulation that modeled the collimation and production  
 301 of the bremsstrahlung photons.

302 The electron beam pulse width was set to 3 ns at a  
 303 repetition rate of 240 Hz with a 1.1 A peak current. The  
 304 3 ns pulse width was small compared to the median neu-  
 305 tron ToF of 80 ns, and thus made a small contribution  
 306 to the uncertainty in the neutron energy determination.  
 307

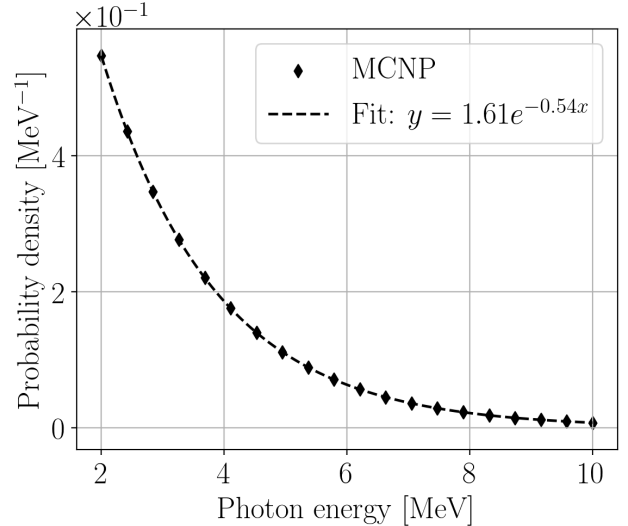


**FIG. 6:** MCNP simulation of the energy distribution of the bremsstrahlung photons that reach the fission target.  
 Photons with an energy below 2 MeV are excluded.

308

309

310

### D. DU Target

311 A depleted uranium (DU) target in the shape of a thin  
 312 strip with dimensions of  $4 \times 2 \times 0.05 \text{ cm}^3$  and a mass of  
 313 7.6 g was used as the primary target.  $^{238}\text{U}$  was chosen as  
 314 the fission target because it is an even-even nucleus, and  
 315 as a consequence, the fission fragments are emitted with  
 316 a high degree of anisotropy with respect to the photon  
 317 beam direction [13].

318 Any target comprised of heavy nuclei has a significant  
 319 potential to scatter fission neutrons before they exit the  
 320 target. This is cause for concern, because neutrons that  
 321 scatter from heavy nuclei are likely to be deflected at  
 322 large angles, resulting in the measurement of  $\theta_{nn}$ 's uncon-  
 323 nected to the underlying fission kinematics. As discussed  
 324 in detail in section V C, an MCNP simulation estimated  
 325 that 6% of reconstructed  $\theta_{nn}$ 's are perturbed due to neu-  
 326 tron scattering within the  $^{238}\text{U}$  target. Moreover, it is  
 327 more likely that neutrons emitted along the wide, 2 cm,  
 328 axis of the  $^{238}\text{U}$  target undergo a scattering event than  
 329 neutrons emitted along the thinnest, 0.05 cm, axis. As  
 330 a result, detectors located collinear to the widest axis of  
 331 the target would see relatively fewer neutrons due to in-  
 332 creased scattering along this axis. This bias is removed  
 333 by slowly rotating the target about the vertical axis dur-  
 334 ing data acquisition at a rate of one rotation per 8 sec-  
 335 onds.

336

### E. Electronics

337 A data acquisition system based on the NIM/VME  
 338 standard was used. A schematic of the data acquisition  
 339 logic is shown in Figure 7. The PMTs are supplied neg-  
 340 ative voltages ranging from 1300 to 1500 V by a LeCroy  
 341 1458 high voltage mainframe. Analog signals from the  
 342 PMTs were fed into a leading edge discriminator (CAEN  
 343 Mod. N841) with input thresholds ranging from 30 mV  
 344 to 50 mV. The threshold and supply voltages were deter-  
 345 mined individually for each detector to minimize noise,  
 346 while simultaneously matching the efficiencies of all the  
 347 detectors as closely as possible. Logic signals from the  
 348 discriminator were converted to ECL logic and fed into a  
 349 CAEN model V1290A TDC. The timing of signals from  
 350 the PMTs were always measured relative to a signal from  
 351 the accelerator provided at the beginning of each pulse.  
 352 Even though a multi-hit TDC was used, only the first  
 353 signal in each pulse from any given PMT was taken into  
 354 account due to concerns over dead-time within the elec-  
 355 tronics and signal reflections within the cables. On the  
 356 software side, the CODA 2.5 [15] software package de-  
 357 veloped by Jefferson Laboratory was used to read out the  
 358 data from the TDC and digitally store it for analysis.

359

## III. MEASUREMENT TECHNIQUES

360

### A. Particle Time of Flight and Energy Determination

361

362 The ToF of detected particles is used to distinguish  
 363 between neutrons and photons as well as determine neu-  
 364 tron energy. A particle's reconstructed position is used  
 365 to determine direction of motion, which is then used to  
 366 calculate the opening angle between pairs of detected par-  
 367 ticles. Position and ToF are each determined using the  
 368 timing of coincident signals from both PMTs of a given  
 369 detector.

370 The sum of the times required for scintillation light  
 371 to travel from the point of scintillation to both PMTs  
 372 is equal to the time required for the light to travel the  
 373 full length of the scintillator, which is a constant for light  
 374 that travels parallel to the length of the scintillator. This  
 375 is supported by data, shown in Fig. 8, which were pro-  
 376 duced from a series of tests in which a collimated  $^{60}\text{Co}$   
 377 source was placed at seven different locations along a  
 378 scintillator. One of the two coincident photons emitted  
 379 by  $^{60}\text{Co}$  reaches the scintillator and the other is detected  
 380 by an auxiliary detector serving as the trigger. The pho-  
 381 tons incident on the scintillator have a spot size of less  
 382 than 1 cm due to source collimation. These events all  
 383 have equal transit time, regardless of the  $^{60}\text{Co}$  source's  
 384 position.

385 In Figure 8(a), it can be seen that the time required  
 386 for the scintillation light to propagate along the scintil-  
 387 lator has a large effect on the timing of each PMT alone,  
 388 however, the average of the times of both PMTs is a con-

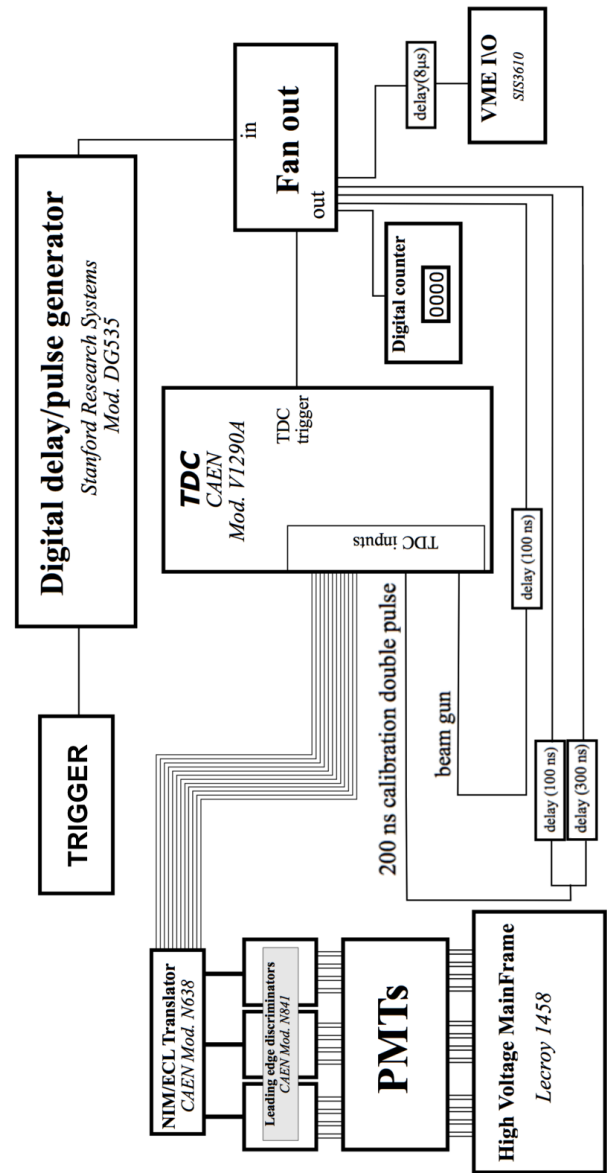


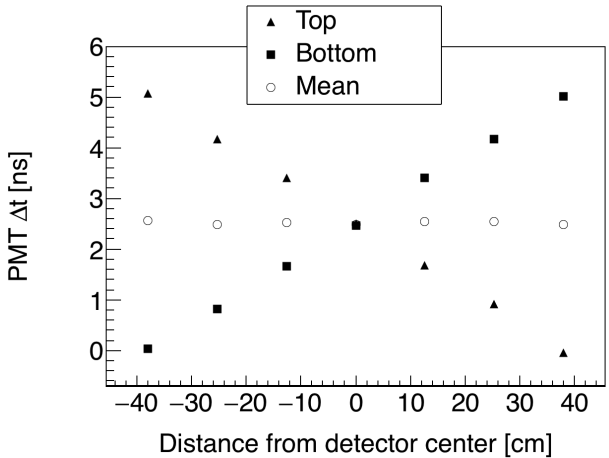
FIG. 7: Wiring diagram of the electronics setup.

389 stant, unaffected by the location at which the particle  
 390 undergoes scintillation. For this reason, taking the aver-  
 391 age of signals from two PMTs is advantageous because it  
 392 removes the roughly 5 ns timing error that would other-  
 393 wise exist due to the time required for scintillation light  
 394 to propagate along the scintillator. The requirement that  
 395 there be coincident events in both of a detector's PMTs  
 396 also aids in reducing noise.

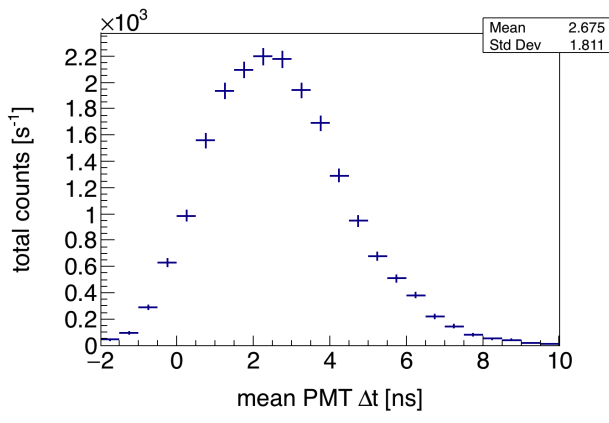
398 During photofission measurements, ToF is calculated  
 399 by the following expression:

$$\text{ToF} = t_{\text{mean}}^{\text{PMTs}} - t_{\text{beam}} + C, \quad (1)$$

400 where  $t_{\text{mean}}^{\text{PMTs}}$  is the mean of the times of signals from  
 401 both PMTs of a scintillator,  $t_{\text{beam}}$  is the time of a sig-  
 402 nal provided by the accelerator at the beginning of each



(a)

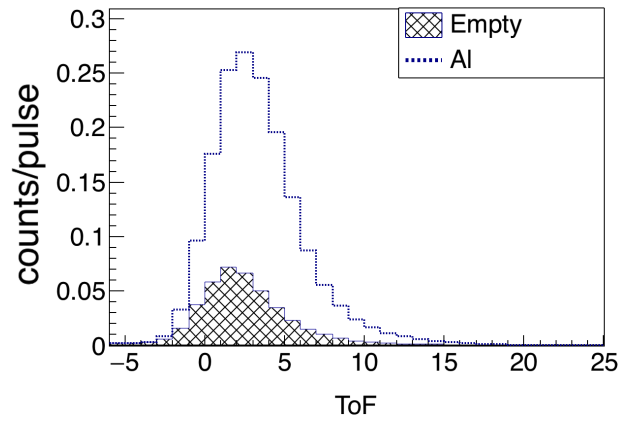


(b)

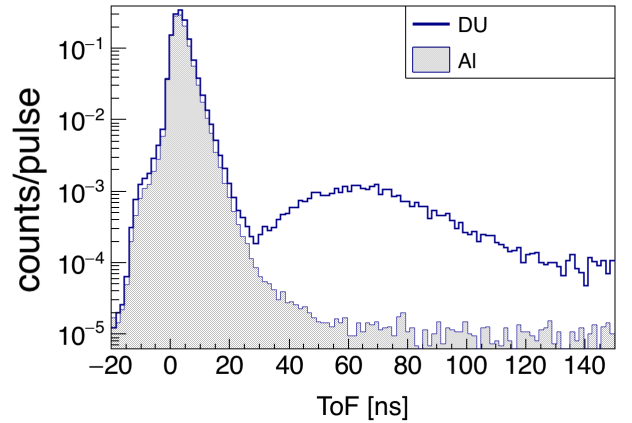
**FIG. 8:** A collimated  $^{60}\text{Co}$  source is used to produce photon events with constant ToF at seven locations along the detector.  $^{60}\text{Co}$  produces coincident photons, and one is detected by the scintillator and the other by a separate trigger detector.  $\Delta t$  is the timing of a PMT signal relative to a signal from the trigger detector. In (a), it can be seen that the average between signals from both PMTs does not depend on position. By using the PMT average, there is a reduction in error due to the time required for scintillation light to travel along the scintillator. The uncertainty in ToF measurements is equal to the standard deviation seen in (b), or about  $\pm 2$  ns, because all photons from the  $^{60}\text{Co}$  source have the same ToF.

403 pulse, and  $C$  is a constant timing offset. Any process that  
404 produces a timing delay that does not change from pulse  
405 to pulse contributes to  $C$ . For example, the time required  
406 for photons to travel from the bremsstrahlung radiator to  
407 the target, the propagation of signals through the cables  
408 connecting the PMTs, delays in the electronics, *etc.*

409 The value of  $C$ , which may be different for each de-  
410 tector, is determined by comparing the timing spectra  
411 of the gamma flash produced by a non-neutron produc-  
412 ing aluminum target, to that produced when no target  
413 is used (see Fig. 9). The difference between these two  
414 spectra reveals a prominent peak in the ToF spectrum



(a)

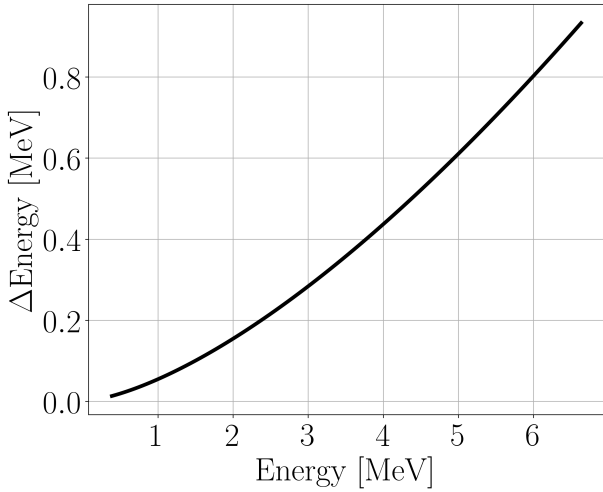


(b)

**FIG. 9:** (a) Comparison between the ToF spectrum of a non-neutron producing target made from Al, to the ToF spectrum produced when no target is used. The large increase in events around 4 ns is due to photons that scatter from the Al target. When no target is in place, sources of the peak seen here is used to find the timing offsets that make it so  $t = 0$  corresponds to the moment of fission. (b) Comparison between the Al and DU targets show a pronounced increase in events for DU between 35 and 130 ns due to the introduction of neutrons.

415 due to photons that scatter from the aluminum target.  
416 These photons must travel 125 cm to reach the center of  
417 any detector and 130 cm to reach the top, for which it  
418 takes light 4.2 ns and 4.3 ns to travel, respectively. The  
419 value of  $C$  used for each detector is equal to the value  
420 that places the time corresponding to the peak of the  
421 target-induced gamma flash at 4 ns.

422 The kinetic energy of a detected neutron is determined  
423 straightforwardly from its velocity, which is determined  
424 from its ToF under the assumption that the neutron trav-  
425 eled directly from the target to the detectors unimpeded.  
426 According to a series of MCNP simulations examining  
427 the scattering of fission neutrons within detector shield-  
428 ing and the fission target, neutrons predominantly travel  
429 to the detectors unimpeded. These simulations are dis-



(a)

**FIG. 10:** Uncertainty in neutron energy measurements as a function of measured neutron energy.

430 cussed in sections IID and IIA.

431 Figure 10 shows the measurement uncertainty in neu-  
432 tron energy due to error in the ToF determination.

### 434 B. Particle Position Reconstruction

435 Each detector is not capable of measuring the position  
436 of a detected particle along the axes parallel to its width  
437 (15.24 cm) or depth (3.81 cm), which contributes  $\pm 3^\circ$  to  
438 the total angular uncertainty. The position of a detected  
439 particle along the 76.2 cm length of the scintillator is  
440 calculated using the timing difference of signals from both  
441 of a detector's PMTs. Assuming that scintillation light  
442 travels from an initial point, let it be  $x$  cm from the  
443 center of a scintillator, to both PMTs at a velocity that  
444 is constant with respect to the scintillator's length-wise  
445 axis, then the difference between the times at which the  
446 light will reach each PMT ( $\Delta t^{PMTs}$ ) is given by:

$$\begin{aligned} \Delta t^{PMTs} &= t^{PMT_1} - t^{PMT_2} \\ &= \frac{(L/2 + x)n_{\text{eff}}}{c} - \frac{(L/2 - x)n_{\text{eff}}}{c} \\ &= 2x \frac{n_{\text{eff}}}{c}. \end{aligned} \quad (2)$$

447 Solving for  $x$  gives

$$x = \frac{c}{2n_{\text{eff}}} \Delta t^{PMTs}, \quad (3)$$

448 where  $t^{PMT_1}$  and  $t^{PMT_2}$  are the times of signals from  
449 each of a detector's PMTs relative to the accelerator gun  
450 pulse,  $L$  is the length of the scintillator,  $c$  is the speed  
451 of light,  $n_{\text{eff}}$  is the effective index of refraction of the  
452 scintillation material. A linear least squares fit between  
453  $x$  and  $\Delta t^{PMTs}$  was performed on data gathered using

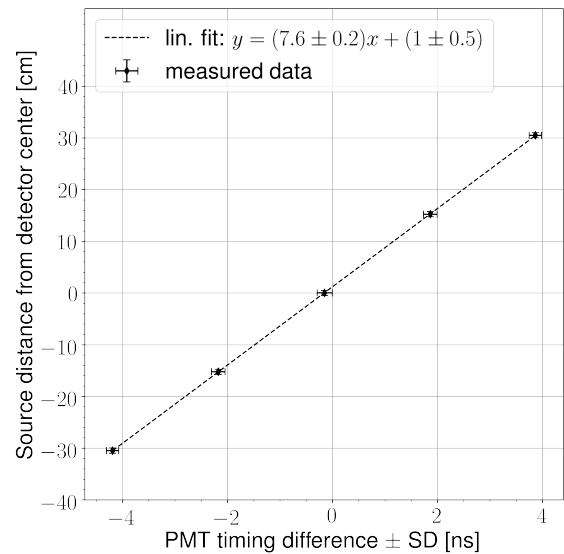


**FIG. 11:** A collimated  $^{60}\text{Co}$  source is used to produce photon events at five different positions along the scintillator. The mean PMT timing difference of events at each position varies linearly with respect to the distance of the  $^{60}\text{Co}$  source from the center of the detector. The result of a linear least squares fit to this data is used to calculate the position of detected particles along the length of each scintillator.

454 coincident photons emitted by a collimated  $^{60}\text{Co}$  source,  
455 as described in the previous section. The resulting fit  
456 parameters, seen in Fig. 11, are used to find the position  
457 of detected particles.

458 Using the slope of the linear fit in Fig. 11, along with  
459 Eq. 3, an effective index of refraction of the scintillation  
460 material is calculated to be 2.0. This index of refraction  
461 is said to be “effective” because its measurement is sen-  
462 sitive only to the scintillation light’s average speed pro-  
463 jected onto the axis parallel to the scintillator’s longest  
464 dimension, which is equal to the intrinsic speed of light  
465 in the material only if the light is traveling parallel to the  
466 scintillator’s length. While the detection of scintillation  
467 light by both PMTs favors light paths which are par-  
468 allel or nearly-parallel to the scintillator’s length, there  
469 is some reflection of detected scintillation light from the  
470 boundaries of the scintillator. This effect contributes to  
471 the  $\pm 9$  cm measurement uncertainty in particle position  
472 reconstruction. As a result of these effects, the index of  
473 refraction measured here is  $\sim 25\%$  greater than the true  
474 value of the scintillation material.

### C. Measurements with $^{252}\text{Cf}$

475 A  $^{252}\text{Cf}$  source was placed at the center of the detec-  
476 tion system shown in Fig. 2 in order to measure the n-n

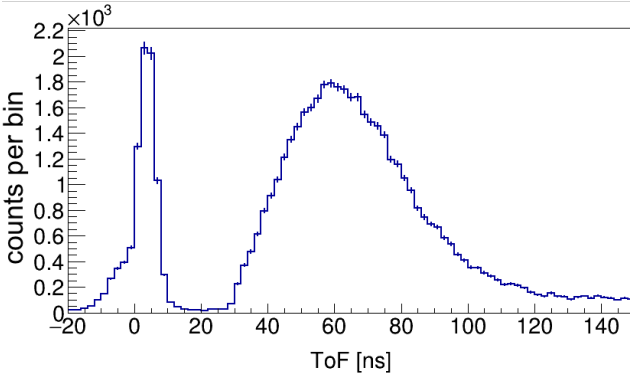


**FIG. 12:** Measured ToF spectrum from the SF of  $^{252}\text{Cf}$ . The sharp peak on the left is due to fission photons, followed by another peak due to fission neutrons.

479 opening angle distribution. Several such past measurements have been performed (see Refs. [7–10]), and serve  
480 as a means to validate the methods used throughout this  
481 study.

482 The  $^{252}\text{Cf}$  source produces a cleaner ToF spectrum  
483 than photofission due to the lack of beam related back-  
484 grounds (see Fig. 12), and therefore these measurements  
485 have a better signal to noise ratio. Also, there is no con-  
486 cern over the detection of accidental neutron coincidences  
487 because the fission rate of the  $^{252}\text{Cf}$  source was about  
488 3,500 fissions/s, making it highly unlikely that multiple  
489 fissions will occur during the electronic acceptance time  
490 window of 150 ns. The beginning of the 150 ns neutron  
491 acceptance time window was triggered by a 2-fold co-  
492 incidence, within a 4 ns window, between two separate  
493  $10 \times 10 \times 5 \text{ cm}^3$  plastic scintillators, one placed above and  
494 the other below the source at a distance of 30 cm. Aside  
495 from this difference in the time window triggering mech-  
496 anism, identical methods were used for both photofission  
497 and SF measurements.

#### IV. ANALYSIS

500 The efficiency and acceptance of the neutron detection  
501 system varies greatly over its opening angle range of  $20^\circ$   
502 to  $180^\circ$ , as illustrated in Fig. 13. This is both due to the  
503 neutron detection system's non-spherical symmetry and  
504 to varying efficiency as a function of particle position on  
505 the detector. In order to give a result that is sensitive  
506 to angular correlations, but is highly insensitive to detec-  
507 tor efficiencies and experimental drifts in PMT voltage,  
508 accelerator current, *etc.*, the angular correlation is deter-  
509 mined by dividing a correlated neutron distribution by  
510 an uncorrelated neutron distribution. That is,

$$\text{angular correlation} = \frac{nn_{\text{corr}}(\theta)}{nn_{\text{uncorr}}(\theta)}, \quad (4)$$

511 where  $nn_{\text{corr}}(\theta)$  is the n-n yield after the subtraction of  
512 accidental n-n coincidences, and  $nn_{\text{uncorr}}(\theta)$  is a con-  
513 trived distribution of uncorrelated n-n pairs, which is  
514 produced by pairing neutron events that occurred dur-  
515 ing different pulses. The subtraction of accidental n-n  
516 coincidences to produce  $nn_{\text{corr}}(\theta)$  amounts to a 10% cor-  
517 rection, the procedure of which is covered in section IV B.  
518 The construction of  $nn_{\text{uncorr}}(\theta)$  is described in detail in  
519 section IV A.

#### 520 A. Cancelation of Detector Efficiencies, Drifts, and 521 Geometric Phase Space

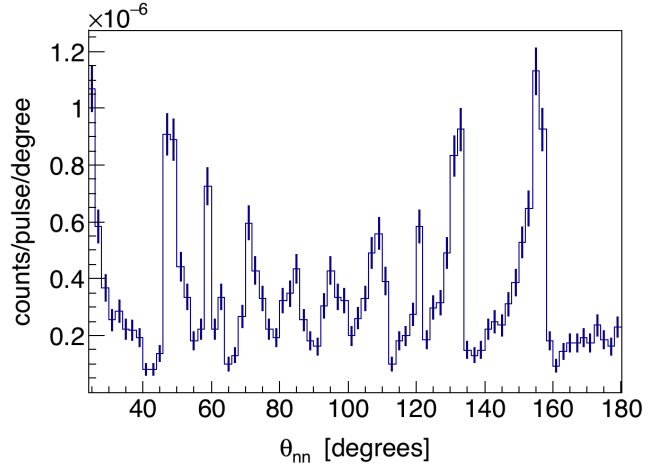


**FIG. 13:** Raw n-n opening angle yield from the photofission of  $^{238}\text{U}$ . This distribution is highly influenced by the detection system's geometric acceptance and efficiency.

522 The construction of  $nn_{\text{uncorr}}(\theta)$  is achieved by pairing  
523 detected neutrons that were produced during different ac-  
524 celerator pulses. The same set of pulses used for  $nn_{\text{corr}}(\theta)$   
525 is used here, so each of these pulses individually consist  
526 of the detection of two coincident neutrons. When con-  
527 structing  $nn_{\text{uncorr}}(\theta)$ , it is desirable that the neutrons  
528 comprising each uncorrelated n-n pair originated from  
529 different pulses that occurred as closely together in time  
530 as possible. A smaller time difference between pulses  
531 that are paired for this purpose increases the chance that  
532 both neutrons were detected under the same experimen-  
533 tal conditions amid any drifting of accelerator current,  
534 PMT voltages, and varying rates of noise. However, some  
535 time difference between the pulses must be allowed so as  
536 not to cause insufficient counting statistics. Accordingly,  
537 uncorrelated n-n pairs used to construct  $nn_{\text{uncorr}}(\theta)$  are  
538 formed by neutrons that were detected within 30 minutes  
539 or less of each other.

540 Uncorrelated n-n pairs will have a slightly different  
541 joint energy distribution than correlated n-n pairs, which  
542 could affect the extent to which the effects of detector  
543 efficiency cancel in Eq. 4. This issue is addressed in sec-  
544 tion V A, where it is shown that these differences have

545 little potential to significantly affect the final result.

546 Figure 14(a) shows the measured yield distribution of  
 547 correlated neutrons,  $nn_{\text{corr}}(\theta)$ , from the photofission of  
 548  $^{238}\text{U}$ . The structure seen here is reflective of the un-  
 549 derlying n-n angular correlations as well as the geomet-  
 550 ric acceptance and efficiencies of the neutron detectors.  
 551 Figure 14(b) reveals how a clear picture of n-n angu-  
 552 lar correlations emerges when taking the ratio between  
 553  $nn_{\text{corr}}(\theta)$  and  $nn_{\text{uncorr}}(\theta)$ . Applying the same technique  
 554 to a measurement of coincident neutrons from the pho-  
 555 todisintegration of  $\text{D}_2\text{O}$  produces a flat line as expected  
 556 (see Fig. 15), as in this case all neutron coincidences are  
 557 accidental.

## 558 B. Subtraction of Accidental Coincidences

559 The observation of two uncorrelated signals in the neu-  
 560 tron ToF range, whether caused by neutrons, photons,  
 561 or noise, is referred to as an *accidental coincidence*. Ac-  
 562 cidental coincidences due to noise and photons, which  
 563 are estimated using a non-neutron producing aluminum  
 564 target (see Fig. 16), amount to about 3% of all coin-  
 565 cidences. Accidental coincidences due to neutrons are  
 566 minimized by adjusting the accelerator's current so that  
 567 there are, on average, less than 1.0 fissions per accelerator  
 568 pulse. Nevertheless, statistical fluctuations in the num-  
 569 ber of fissions per pulse result in the production of acci-  
 570 dental coincident neutrons that originated from different,  
 571 and therefore, uncorrelated fissions. There are also ac-  
 572 cidental neutron coincidences caused by the occurrence  
 573 of multiple  $(\gamma, n)$  reactions in a single pulse. The energy  
 574 integrated  $(\gamma, n)$  cross-section of  $^{238}\text{U}$ , weighted by the  
 575 bremsstrahlung energy distribution, is about a factor of  
 576 5.5 times greater than it is for photofission (see Fig. 17).  
 577 As a result, the raw n-n coincident yield will contain a sig-  
 578 nificant number of n-n coincidences from multiple  $(\gamma, n)$   
 579 reactions in relation to n-n coincidences from fission. The  
 580 presence of accidental n-n coincidences has the effect of  
 581 washing out the signal from correlated neutrons.

582 The raw measurement of n-n yield consists of a mix of  
 583 correlated and accidental neutron coincidences, that is

$$584 nn_{\text{raw}}(\theta_{nn}) = nn_{\text{corr}}(\theta_{nn}) + nn_{\text{acc}}(\theta_{nn}), \quad (5)$$

586 where  $nn_{\text{raw}}(\theta_{nn})$  and  $nn_{\text{acc}}(\theta_{nn})$  are the per-pulse n-n  
 587 yields as a function of opening angle,  $\theta_{nn}$ , for all detected  
 588 n-n pairs, and detected accidental n-n pairs, respectively.  
 589 As already defined,  $nn_{\text{corr}}(\theta_{nn})$  is the per-pulse yield of  
 590 detected correlated n-n pairs.

591 Because the n-n coincidences comprising  $nn_{\text{acc}}(\theta_{nn})$   
 592 consist of two independent detected neutrons, they are  
 593 governed by the exact same physics and are subject to  
 594 the exact same experimental conditions as n-n coinci-  
 595 dences formed by pairing of single neutrons that were  
 596 detected during different pulses. Therefore, the open-  
 597 ing angle distribution formed by pairing neutrons that  
 598 were detected during different pulses, denoted  $nn_{dp}(\theta_{nn})$ ,

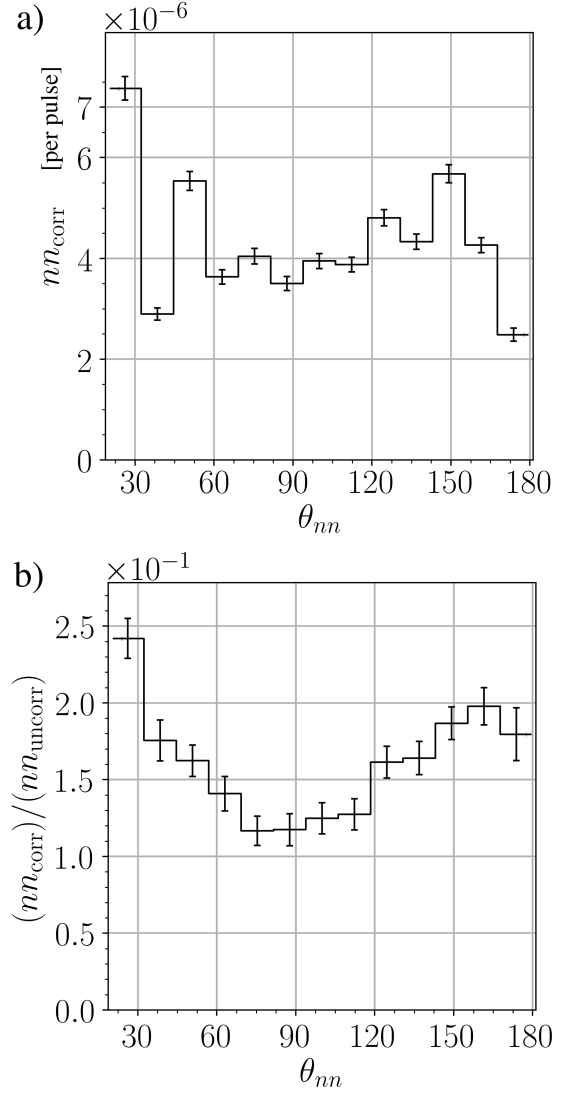
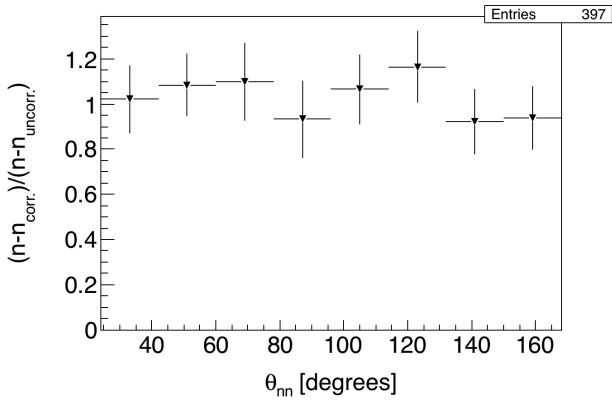


FIG. 14: n-n opening angle distribution from the photofission of  $^{238}\text{U}$  before the normalization procedure seen in Eq. 4 (a), and after normalization (b). All measured neutrons have an energy greater than 0.4 MeV.

599 is proportional to  $nn_{\text{acc}}(\theta_{nn})$ .  $nn_{dp}(\theta_{nn})$  is constructed  
 600 from the set of all possible pulse-pairs formed by pulses  
 601 that occurred within 0.2 seconds of each other. The re-  
 602 striction in time difference is applied in order to increase  
 603 the chance that pulse pairs together occurred under sim-  
 604 ilar experimental conditions. There are no other restric-  
 605 tions on which pulses can be used in this case. Many  
 606 pulse-pairs used for the construction of  $nn_{dp}(\theta_{nn})$  will  
 607 contain no detected neutrons.

608 While  $nn_{dp}(\theta_{nn})$  and  $nn_{\text{acc}}(\theta_{nn})$  are proportional,  
 609  $nn_{\text{acc}}(\theta_{nn})$  is not equal to  $nn_{dp}(\theta_{nn})$ , because there are,  
 610 on average, more detected neutrons per pulse-pair than



**FIG. 15:** A measurement of the angular correlation of uncorrelated neutrons emitted by the photodisintegration of  $\text{D}_2\text{O}$  gives the expected uniform distribution.

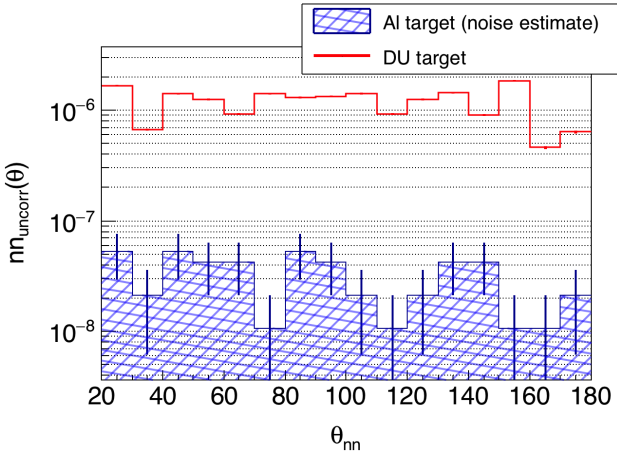


**FIG. 16:** An Al target was designed have the same thickness, in radiation lengths, as the  $^{238}\text{U}$  target, thus serving as an equivalent non-neutron producing target well-suited for noise estimates. The rate of the detection of coincident events in the neutron ToF range while using the Al target was 3% that of the  $^{238}\text{U}$  target. Thus, 3% of coincident events used in the determination of n-n angular correlations in  $^{238}\text{U}$  can be attributed to noise.

per pulse. As the following analysis shows,  $nn_{\text{acc}}(\theta_{nn}) = \frac{1}{2}nn_{dp}(\theta_{nn})$ , under the condition that  $nn_{\text{acc}}(\theta_{nn})$  is normalized to the number of pulses and  $nn_{dp}(\theta_{nn})$  to the number of pulse-pairs considered. When looking at single pulses, the probability of there being a detected uncorrelated n-n pair is denoted by  $P_{\text{sp}}^{\text{n-n}}$ , and when looking at pulse-pairs, by  $P_{\text{dp}}^{\text{n-n}}$ . Thus,  $P_{\text{sp}}^{\text{n-n}}$  and  $P_{\text{dp}}^{\text{n-n}}$  determine the relative rates of  $nn_{\text{acc}}(\theta_{nn})$  and  $nn_{dp}(\theta_{nn})$ , respectively. The statistics of the detected uncorrelated neutrons per pulse is assumed to follow a Poisson distribution, which describes the occurrence of independent random events. Accordingly, the probability of the detection of  $k$  uncorrelated neutrons in a given pulse is

$$p(k) = \frac{e^{-\lambda} \lambda^k}{k!}, \quad (6)$$

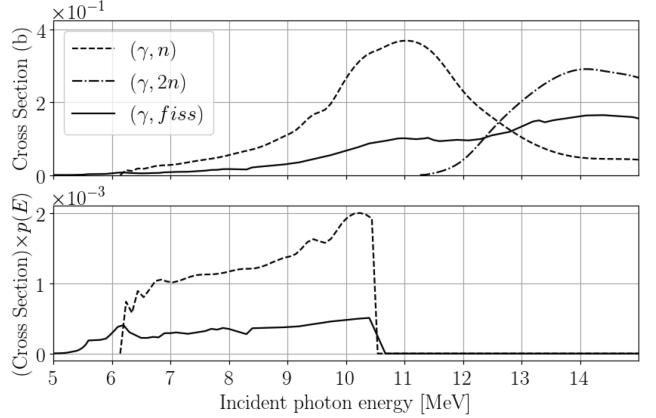


**FIG. 17:** (top) ENDF cross-sections of  $(\gamma, \text{fiss})$ , direct  $(\gamma, \text{n})$ , and direct  $(\gamma, 2\text{n})$ . (bottom) Cross-sections weighted by the simulated relative rate of bremsstrahlung photons that reach the target as a function of photon energy. The integrated cross-sections of  $(\gamma, \text{n})$  is 5.5 times greater than for  $(\gamma, \text{fiss})$ . Assuming a  $\bar{\nu}$  of 2 neutrons/fission, the bremsstrahlung beam produces about 2.7 times more neutrons via  $(\gamma, \text{n})$  than  $(\gamma, \text{fiss})$  within the target.

where  $\lambda$  represents the mean number of uncorrelated detected neutrons per pulse. In principle,  $\lambda$  equals the total number of detected uncorrelated neutrons divided by the total number of pulses. Determination of  $\lambda$  cannot be done in practice, because one would need to know which pairs of detected neutrons are correlated. However, the largest possible value for  $\lambda$  is the total number of detected neutrons divided by the total number of pulses, as this quantity counts all detected neutrons, whether they are correlated or uncorrelated. For this work, that places an upper bound on  $\lambda$  of  $5.5 \times 10^{-3}$  detected uncorrelated neutrons per pulse, which is small enough to truncate all terms beyond the leading term in the following analysis.

Because  $P_{\text{sp}}^{\text{n-n}}$  represents the probability of the detection of two uncorrelated neutrons in a single pulse,  $P_{\text{sp}}^{\text{n-n}}$  is equal to  $p(2)$ , as per Eq. 6. Thus,

$$\begin{aligned} P_{\text{sp}}^{\text{n-n}} &= \frac{e^{-\lambda} \lambda^2}{2!} \\ &\approx \frac{\lambda^2}{2} + \mathcal{O}(\lambda^3). \end{aligned} \quad (7)$$

When considering the case of  $P_{\text{dp}}^{\text{n-n}}$ , recall that, in this case, uncorrelated n-n pairs are formed by examining pulse-pairs. Here, an uncorrelated n-n pair occurs when there is a detected neutron in both pulses. Because all terms beyond the leading term are being truncated, pulse-pairs in which one or both of the pulses comprise two or more detected neutrons do not need to be considered. Thus,  $P_{\text{dp}}^{\text{n-n}}$  is equal to the probability of there being exactly one detected neutron in each pulse, which is the square of the probability of there being exactly one detected neutron in a single pulse, namely,  $p(1)^2$ . Thus,

651 again using Eq. 6,

$$\begin{aligned} P_{dp}^{n-n} &= (e^{-\lambda} \lambda)^2 \\ &\approx \lambda^2 + \mathcal{O}(\lambda^3). \end{aligned} \quad (8)$$

652 Because  $P_{dp}^{n-n}$  and  $P_{sp}^{n-n}$  determine the relative rates of  
653  $nn_{dp}(\theta_{nn})$  and  $nn_{acc}(\theta_{nn})$ , respectively, and because the  
654 two distributions have the same shape, from Eq.'s (8)  
655 and (7), it follows that

$$nn_{acc}(\theta_{nn}) = \frac{1}{2} nn_{dp}(\theta_{nn}). \quad (9)$$

656 Finally, from Eq.'s 9 and 5, the distribution of solely  
657 correlated n-n pairs can be recovered from the raw mea-  
658 surement as follows

$$nn_{corr}(\theta_{nn}) = nn_{raw}(\theta_{nn}) - \frac{1}{2} nn_{dp}(\theta_{nn}). \quad (10)$$

## 659 V. POTENTIAL SOURCES OF ERROR

### 660 A. Correlated versus uncorrelated n-n energy 661 distribution

662 In order to effectively minimize the dependence of the  
663 result on detector geometry/efficiency, the numerator  
664 and denominator of Eq. 4 must comprise neutron pairs  
665 with a similar energy distribution. Note that accidental  
666 coincident neutrons from  $(\gamma, n)$  are completely removed  
667 from  $nn_{corr}(\theta)$ , the numerator in Eq. 4, by the subtrac-  
668 tion of accidental coincidences, but are not removed from  
669 the denominator,  $nn_{uncorr}(\theta)$ . This is the reason for us-  
670 ing only pulse-pairs that have two events in each pulse  
671 when determining the uncorrelated neutron distribution.  
672 Doing so increases the selection of neutrons from fission  
673 as opposed to  $(\gamma, n)$ .

674 When examining differences between the neutron en-  
675 ergy distributions in  $nn_{corr}(\theta)$  and  $nn_{uncorr}(\theta)$ , it is im-  
676 portant to consider how the energies of both neutrons  
677 forming n-n pairs vary together, or, in other words, their  
678 joint energy distribution. Figure 18 shows the ratio be-  
679 tween the rates for correlated and uncorrelated n-n pairs  
680 of various binned energies. The effect that these discrep-  
681 ancies in energy distribution have on the final result can  
682 be examined by applying a weighting factor to each event  
683 in  $nn_{uncorr}(\theta)$  such that a recalculation of the result in  
684 Fig. 18 produces a flat curve. A comparison of the angu-  
685 lar correlation with and without the application of these  
686 weighting factors to uncorrelated n-n events is seen in  
687 Fig. 19. The resulting weighted distribution is identical  
688 within experimental uncertainties to the unweighted dis-  
689 tribution, suggesting that differences in the energy distri-  
690 butions of  $nn_{corr}(\theta)$  and  $nn_{uncorr}(\theta)$  do not significantly  
691 affect the present measurement.

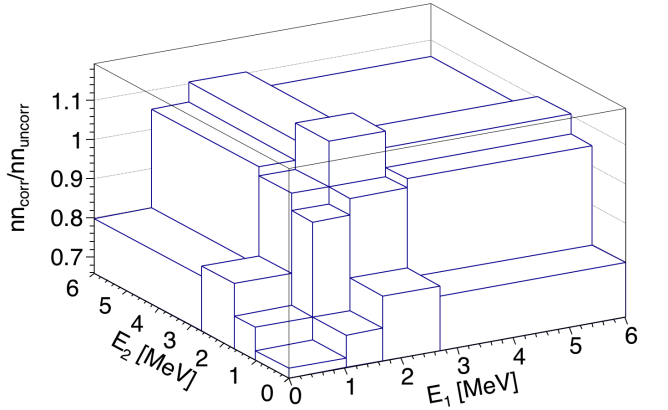


**FIG. 18:** The z-axis represents the ratio between the correlated and uncorrelated rates of binned n-n energies. The energy bins are chosen such that each contains an equal number of events, or 1/16th of the total events.

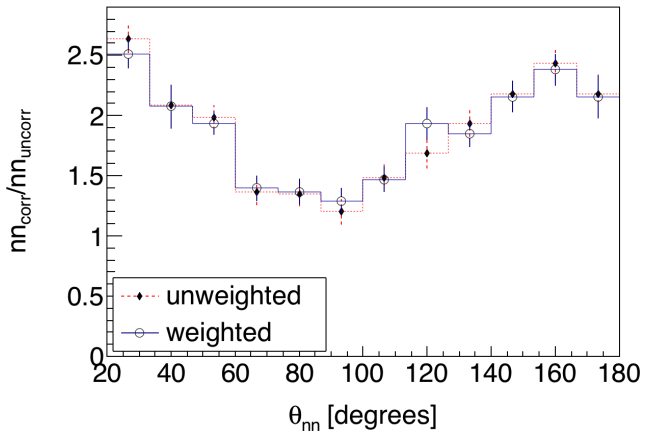


**FIG. 19:** Each uncorrelated n-n event can be weighted such that the weighted histograms of the joint n-n energy distributions of correlated and uncorrelated n-n pairs are equal. Comparison of the calculated angular correlation results, with and without such weighting factors applied to all uncorrelated n-n events, illustrates that any effects due to the discrepancies in the joint energy distributions of correlated and uncorrelated n-n pairs are negligible.

### 694 B. Detector Cross-talk

695 *Cross-talk* occurs when, after a particle is detected  
696 once, the same particle, by any means, causes a detec-  
697 tion to be registered in a different detector. For example,  
698 upon detection, a particle may undergo elastic scattering  
699 and then travel into another detector where it is detected  
700 again, or, it may produce secondary particles that are  
701 detected. The two coincident detections of a cross-talk  
702 event are causally correlated, and thus they have the po-  
703 tential to contaminate the signal from correlated fission  
704 neutrons. If both detections occur during the ToF range  
705 typical for fission neutrons, then the cross-talk event can-  
706 not be distinguished from the detection of two correlated

707 neutrons.

708 Recent works that measured the n-n angular correlations in the spontaneous fission of  $^{252}\text{Cf}$  and  $^{240}\text{Pu}$  [10, 12] 709 addressed this effect by using an MCNP-PoLiMi simulation 710 to estimate and then subtract cross-talk from their 711 measurements. In this work, the issue of cross-talk is 712 approached differently by employing the use of detector 713 shielding aimed at reducing cross-talk to a negligible rate. 714 By using shielding to reduce cross-talk, this measurement 715 is less dependent on the details of the models used by 716 MCNP-PoLiMi to simulate neutron transport and detec- 717 tion. MCNP-PoLiMi simulations are used in this work 718 only to verify that the effect of cross-talk is negligible. 719

720 The scintillators used here are much larger than those 721 used in similar works, such as in Refs. [10, 12], allowing 722 them to be placed much farther from the fission source 723 without causing a detrimental loss in coincidence rates. 724 An increase in the distance between the detectors and 725 the fission source makes this measurement less subject to 726 angular uncertainty, which depends directly on the un- 727 certainty in the position of a detected particle due to, for 728 example, the scattering of neutrons from detector shield- 729 ing. For this reason, larger amounts of shielding can be 730 used without concern of introducing large errors.

731 Furthermore, the geometry of the neutron detection 732 system makes it kinematically impossible for a neutron 733 to undergo a single scattering event with a proton in one 734 detector, which is the basis for scintillation, and then 735 travel directly into another detector with enough kinetic 736 energy to be detected a second time. For this reason, 737 upon being detected, a neutron must scatter from one or 738 more intermediate nuclei, such as lead or carbon, in or- 739 der for it to reach another detector with enough energy 740 to be detected again. This fact follows from the con- 741 servation of energy and momentum. In order to support 742 the claim that the design of the neutron detection system 743 reduced cross-talk to negligible rates, a detailed MCNP- 744 PoLiMi [16] simulation was performed in which a built-in 745  $^{252}\text{Cf}$  source is positioned at the center of a model of the 746 neutron detection system.

### 747 1. Simulation of Detector Cross-talk

748 The cross-talk simulation included all scintillators, 749 shielding, detector supporting structures, and the con- 750 crete walls surrounding the experimental cell. MCNP- 751 PoLiMi's built-in  $^{252}\text{Cf}$  spontaneous fission source was 752 used, which emits neutrons with the correct correla- 753 tions and multiplicities according to previous measure- 754 ments. Detector response was modeled using a program 755 included with the MCNP-PoLiMi distribution called MP- 756 Post [17]. The model is based on the MeV electron equiv- 757 alent (MeVee) light output produced by particles as they 758 undergo collisions with carbon and hydrogen within or- 759 ganic plastic scintillators. A minimum deposited energy 760 of 0.4 MeV (equivalent to 0.05 MeVee for neutrons) was 761 assumed for detectable particles, which was chosen be-

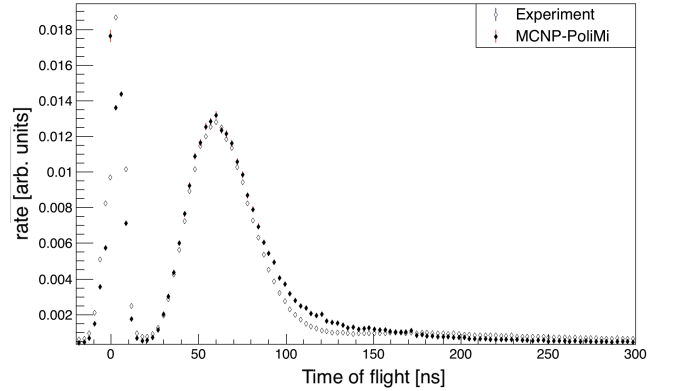


**FIG. 20:** Measured *versus* simulated ToF spectrum from the SF of  $^{252}\text{Cf}$ . The simulation used the detector response model outlined in ref [17]. The simulated and measured curves are normalized in order to facilitate comparison.

762 cause the neutron detection system exhibited a sharp de- 763 cline in detection efficiency for neutrons below 0.4 MeV.

764 For neutron collisions with hydrogen, the light output 765 in MeVee, denoted  $L$ , is calculated by the following em- 766 pirically derived formula [17]

$$L = 0.0364\Delta E_n^2 + 0.125\Delta E_n ,$$

767 where  $\Delta E_n$  is equal to the loss in the kinetic energy of the 768 neutron due to the collision. Neutron interactions with 769 carbon are assumed to generate a small light output of

$$L = 0.02\Delta E_n .$$

770 As seen in Fig. 20, this model of the detection process 771 produces a ToF spectrum for the SF of  $^{252}\text{Cf}$  that shows 772 good agreement with the measurement for neutrons with 773 a ToF less than 100 ns and fair agreement for neutrons 774 with a ToF greater than 100 ns.

776 Figure 21 shows the distribution of cross-talk events 777 and true n-n coincidences as a function of reconstructed 778 opening angle. It is worth noting that, according to this 779 simulation, the effect of cross-talk is not only small, but 780 is also distributed over a wide range of n-n opening angles 781 rather than being concentrated around 0 degrees as one 782 might expect. Angles greater than 125 degrees are not 783 shown in Fig. 21 because cross-talk events at large an- 784 gles can be readily identified in analysis due to the large 785 amount of time required for a neutron to travel these 786 distances. The simulation was initially performed with 5 787 cm of lead shielding placed behind the scintillators, and 788 the number of cross-talk events accounted for 11% of the 789 total coincident neutron events. This value fell to 3% 790 when polyethylene was used instead of lead, motivating 791 the placement of 10 cm of polyethylene behind the de- 792 tectors instead of lead.

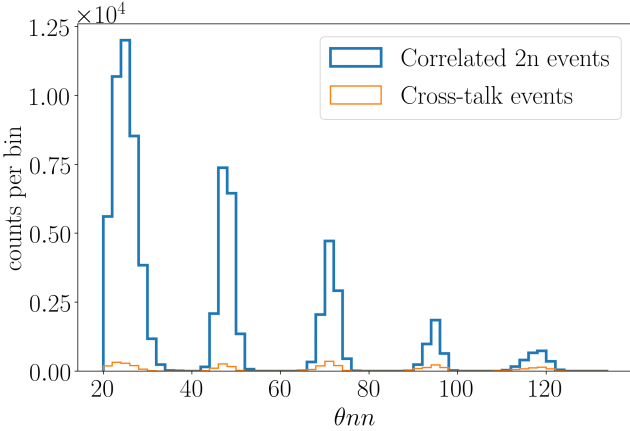


**FIG. 21:** MCNP-PoLiMi simulation of the number of cross-talk events *versus* correlated n-n events as a function of reconstructed opening angle. Cross-talk accounted for 3% of total events. Simulated cross-talk events do not occur primarily at small angles, but are instead spread out over a wide range of angles. Any cross-talk occurring at angles larger than  $125^\circ$  will be removed from the experimental data by the cuts applied to neutron ToF.

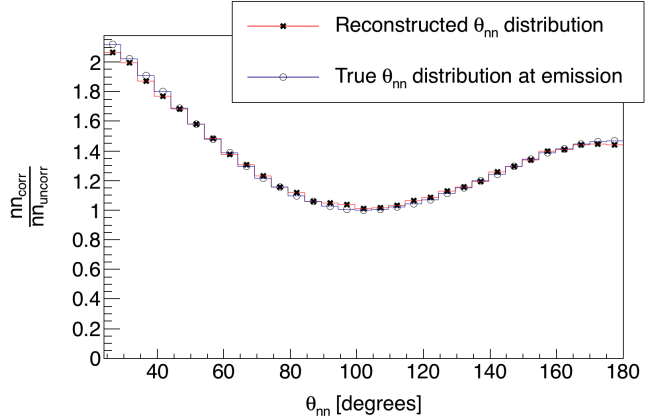


**FIG. 22:** MCNP-PoLiMi simulation of correlated  $^{252}\text{Cf}$  neutrons sampled uniformly throughout a  $0.05 \times 2 \times 4 \text{ cm}^3$  U-238 target. The slight difference between the curves is due solely to the elastic scattering of neutrons within the target, since detector physics was not simulated. In the reconstructed  $\theta_{nn}$  distribution ( $\star$ ), only neutrons which enter a physical volume at which a detector was located during the experiment are counted. The true  $\theta_{nn}$  distribution at the moment of emission is also plotted ( $\circ$ ).

### 794 C. Neutron Scattering within the Target

795 A potential source of error in opening angle measurements is the scattering of emitted neutrons as they tra-  
796 vers the fission target. This is cause for concern because  
797 when neutrons scatter from heavy nuclides such as  $^{238}\text{U}$ ,  
798 they are likely to be deflected at large angles resulting in  
799 n-n opening angles that do not reflect the true underlying  
800 fission kinematics. The effect that this has on this work  
801 is assessed by MCNP simulations. In summary, for 6% of  
802 n-n pairs, at least one neutron out of the two scatters be-  
803 fore exiting the target, according to the simulation. This  
804 effect does not have a large influence on the measured  
805  $\theta_{nn}$  distribution according to the simulation data shown  
806 in Fig. 22.

807 The rate of elastic scattering is affected by the size  
808 and shape of the target. A thin strip is the ideal target  
809 shape regarding the rate of neutron elastic scattering per  
810 unit of total target volume. See Fig. 23 for the simulated  
811 elastic scattering rates for both thin strip and cylindrical  
812 shaped targets. The simulation indicates that the rate of  
813 elastic scattering in cylindrical targets is about a factor  
814 of two times greater than in thin strip targets with the  
815 same volume.

816 The target's dimensions are small enough that the  
817 rate of photon absorption, and thus photo-neutron pro-  
818 duction, is virtually uniform throughout the entire tar-  
819 get volume. An MCNP-PoLiMi simulation was used  
820 to generate  $^{252}\text{Cf}$  spontaneous fission events uniformly  
821 throughout the target. The SF of  $^{252}\text{Cf}$  is used instead  
822 of the photofission of  $^{238}\text{U}$  because of the current lack  
823 of photofission models, however, the underlying fission  
824 kinematics are, broadly speaking, the same for the SF of  
825  $^{252}\text{Cf}$  and the photofission of  $^{238}\text{U}$ . Thus, the two pro-

826 cesses have similar n-n correlations.

827 Section VI B discusses the observation of an unex-  
828 pected drop in correlation around  $180^\circ$  n-n opening an-  
829 gle for the photofission of  $^{238}\text{U}$ , as seen in Figs. 24 and  
830 25. This motivated a second simulation regarding elastic  
831 scattering which examined whether this decrease in the  
832 correlation around  $180^\circ$  opening angles reflects the un-  
833 derlying physics of the fission process. In particular, note  
834 that throughout these measurements, the target was con-  
835 tinuously rotated once per 8 seconds. This means that for  
836 the determination of the uncorrelated opening angle dis-  
837 tribution, the trajectories of the two neutrons were taken  
838 from two different pulses in which the target was at a dif-  
839 ferent orientation for each of them. Additionally, each of  
840 the neutrons likely originated from different regions of the  
841 target volume. On the other hand, for the same-pulse,  
842 correlated neutron measurement, the target was in the  
843 same orientation and the two neutrons were generated  
844 at the same position in the target. For these reasons,  
845 the rates of neutron scattering within the target are not  
846 necessarily equal for the same-pulse and different-pulse  
847 cases. As such, we investigated whether these differences  
848 could cause this apparent decrease in the opening angle  
849 distribution near  $180^\circ$ .

850 Using the correlated  $^{252}\text{Cf}$  SF source built-in to  
851 MCNP-PoLiMi, the opening angle distribution of neu-  
852 trons at the moment of emission, labeled *true* in Fig. 22,  
853 were compared to that of the neutrons after they have es-  
854 caped the target, labeled *reconstructed* in Fig. 22. The lo-  
855 cation of fission events were sampled uniformly through-  
856 out the target's volume. The analysis employs the same  
857 technique outlined in section IV A, in which a correlated  
858 neutron distribution is divided by an uncorrelated neu-

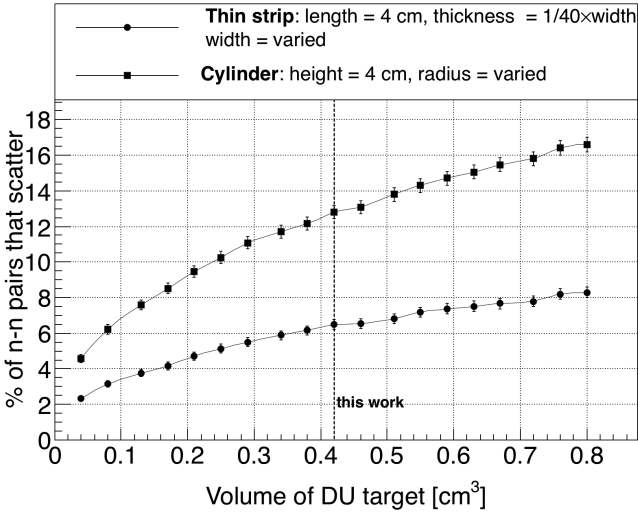


**FIG. 23:** Result of an MCNP simulation in which n-n pairs, with energies sampled from a typical watt fission spectrum, were generated uniformly throughout the volume of DU targets. The y-axis is the rate of opening angle contamination due to the scattering of, within the DU target in which they were produced, either one or both of a pair of neutrons. The lack of symmetry of a thin strip target can be removed by slowly rotating the target around the vertical axis during data acquisition, making it the optimal target geometry for the minimization of the rate of neutron scattering. The target used in this work had a length of 4 cm, a width of 2 cm, and a thickness of 0.05 cm.

tron distribution. The correlated neutron distribution is formed by pairing neutrons emitted during the same fission, and the uncorrelated distribution by the pairing of neutrons emitted during different fissions. In order to account for the effect of a rotating target on the trajectories of neutrons from different pulses, the coordinate system was rotated about the vertical axis accordingly for different fission events. The result from this simulation suggests that the rotating  $0.05 \times 2 \times 4 \text{ cm}^3$  U-238 target does not, due to neutron scattering, result in a measurable departure from the true n-n opening angle distribution.

## VI. RESULTS

### A. Comparisons with FREYA

The n-n opening angle correlation is calculated using the methods outlined in Sec. IV, in which a correlated neutron yield is divided by an uncorrelated yield. The results are compared with output from FREYA [18] (Fission Reaction Event Yield Algorithm), which was developed by the collaborative efforts of researchers from Lawrence Berkeley National Laboratory, Lawrence Livermore National Laboratory, Los Alamos National Laboratory, and University of Michigan Nuclear Engineering, and has been included in MCNP beginning with version

### 6.2.

The most recent release of FREYA (version 2.0.3) does not contain photofission directly, but instead uses neutron-induced fission as an *ad hoc* photofission model [19]. Representing photofission in this manner is a crude approximation, unsupported by experimental verification. Nonetheless, due to the current lack of accepted photofission models, the approximate approach, included in FREYA version 2.0.3, is compared with the results of the present work.

For a given nucleus with Z protons and A total nucleons, the code selects the neutron-induced fission model for a Z(A-1) nucleus, and chooses an incident neutron energy such that the compound ZA nucleus will have, relative to ZA's ground state, an excitation energy that is equal to the energy of the would-be incident photon.

When using FREYA to model photofission in this work, all model parameters, such as level density and partition parameters, were set to their default values for neutron-induced fission. FREYA was configured to use the fission fragment mass distribution,  $Y(A)$ , and the average total kinetic energy,  $\langle \text{TKE} \rangle(A)$ , from the  $^{238}\text{U}$  photofission measurements described in Ref. [20].

The measured  $\theta_{nn}$  distribution from the photofission of  $^{238}\text{U}$  and the SF of  $^{252}\text{Cf}$  are presented with the following two different types of cuts applied to the energies of neutrons in coincidence: in Figs. 24 ( $^{238}\text{U}$ ) and 26 ( $^{252}\text{Cf}$ ), a minimum energy threshold is applied to both neutrons, and in Figs. 25 ( $^{238}\text{U}$ ) and 27 ( $^{252}\text{Cf}$ ), the energy of both neutrons are required to fall within a specified range

In each of Figs. 24 through 27, the data are reported using two representations: the classic histogram and the kernel density estimate (KDE). When using a histogram to estimate a continuous distribution from the relatively small number of data points obtained in this work, one faces the following dilemma: small bin-widths lead to large uncertainties that are dependent on the chosen bin-width, while large bin-widths obscure potentially useful information. This problem is mitigated by the use of a KDE. A KDE is a method for estimating a continuous probability distribution from a finite set of sampled data points. The kernel was chosen to be the measurement errors in opening angle as determined by a study using coincident photons from a  $^{60}\text{Co}$  source, which was placed at different locations along a detector. The measurement errors in  $\theta_{nn}$  are well-described by a gaussian with a standard deviation of  $6^\circ$ . Mathematical details of the KDE method used in this work are outlined in Ref. [21]. The error bands seen in Figs. 24 through 27 correspond to 68% confidence intervals.

Plotted with each measurement is the result of a FREYA simulation. For the measurement of  $^{238}\text{U}$  photofission, there were a total of 2,952 n-n coincident events after the subtraction of accidentals, and for the SF of  $^{252}\text{Cf}$ , there were 21,882.

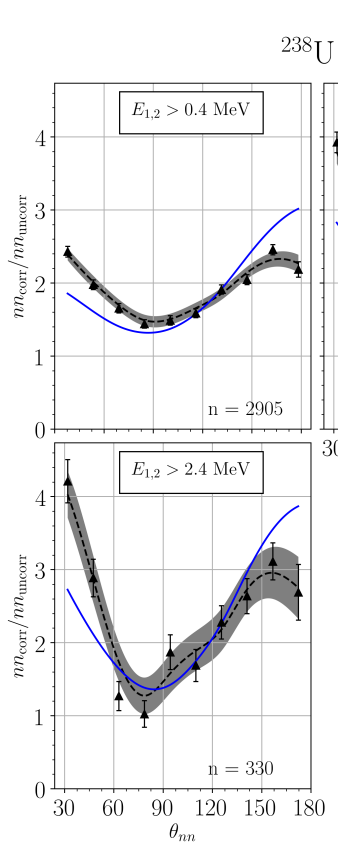


**FIG. 24:**  $\theta_{nn}$  distribution with minimum neutron energy cuts applied. The number of events contributing to each plot,  $n$ , is shown. Note that the bottom plots of this figure and Fig. 25 are identical.

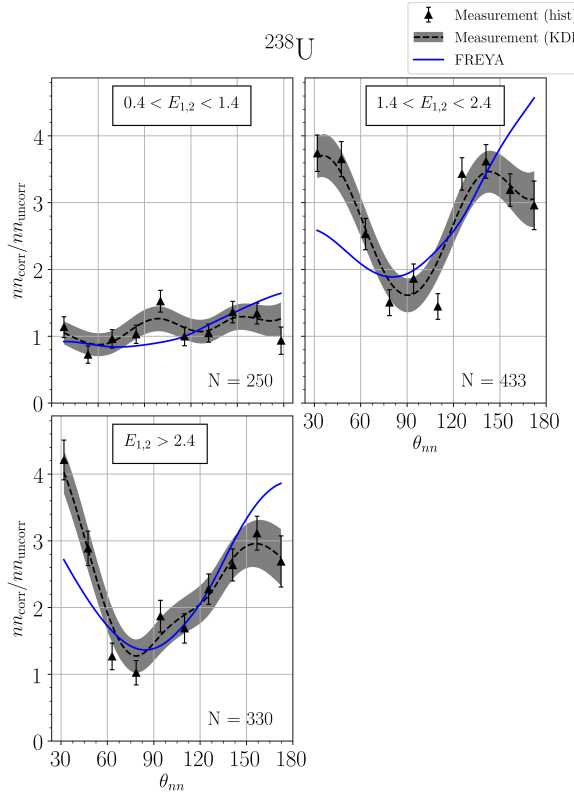


**FIG. 25:**  $\theta_{nn}$  distribution with cuts requiring that the energy of both coincident neutrons be within the specified range. The number of events contributing to each plot,  $N$ , is shown. Note that the bottom plots of this figure and Fig. 24 are identical.

## 941 B. Anomalous emission at large opening angles

942 While the results reported in the previous section are  
943 consistent with the effect of the kinematic focusing of the  
944 neutrons due to the recoil of the fission fragments, the  
945 data for U-238 show a statistically significant decrease  
946 in the n-n opening angle correlation in the region from  
947 about  $165^\circ$  to  $180^\circ$ , which can be seen in Figs. 14 and  
948 30, as well as in Figs. 24 and 25. The effect is particularly  
949 strong for the neutron energy cuts being applied in the  
950 upper right plots of both Figs. 24 and 25. A comparison  
951 of the observed decrease after  $160^\circ$  degrees with the null  
952 hypothesis that the true distribution remains constant  
953 after  $160^\circ$  degrees yields a p-value of 0.01. This indicates  
954 a 1% probability that the data are incompatible with a  
955 decrease in the correlation for large opening angles. This  
956 is a feature which does not seem to universally appear  
957 in either neutron-induced or spontaneous fission. A sim-  
958 ilar but less pronounced effect appears in the results re-  
959 ported in Ref. [11] for the thermal neutron-induced fission  
960 of  $^{233}\text{U}$  and  $^{235}\text{U}$ , but not for the spontaneous fission of  
961  $^{252}\text{Cf}$  or the neutron-induced fission of  $^{239}\text{Pu}$ . The promi-  
962 nence of this effect observed in the present work may be a

963 characteristic feature of the photofission of the even-even  
964  $^{238}\text{U}$  nucleus.

965 Interesting effects are also seen when plotting neutron  
966 correlation *versus* energy for several different opening an-  
967 gle cuts. Fig. 28 top shows the correlation when a min-  
968 imum threshold is applied to the absolute difference in  
969 the energies of coincident n-n pairs. Note that a suppres-  
970 sion of correlated emission for large opening angles only  
971 occurs in n-n pairs that have a large difference in energy,  
972 as indicated by Fig. 28 top.

973 While a definitive explanation of these results would  
974 be greatly aided by detailed modeling studies, these data  
975 are consistent with two possible explanations relating to  
976 the unique feature of the asymmetric angular emission  
977 of fission fragments in photofission. First, the neutrons  
978 may indeed be emitted isotropically in the rest frame of  
979 the fission fragment, but one fragment essentially shad-  
980 ows the neutrons emitted from the other fragment, either  
981 through absorption or scattering, leading to a decrease in  
982 emission along the fission axis. The decrease in corre-  
983 lation at  $\theta_{nn}$ 's greater than  $170^\circ$  for n-n pairs with a large  
984 energy difference, as seen in Fig. 28 top, is consistent with  
985 the proposed shadowing mechanism for the case of neu-  
986 tron pairs emitted along the fission axis from the same

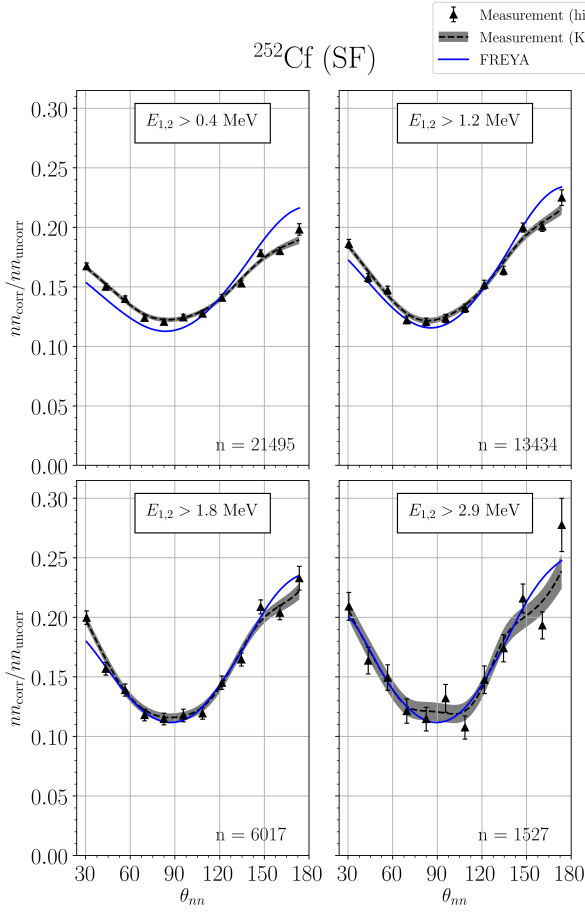


**FIG. 26:**  $\theta_{nn}$  distribution with minimum neutron energy cuts applied. The number of events contributing to each plot,  $n$ , is shown. Note that the lower right plots of this figure and Fig. 27 are identical.

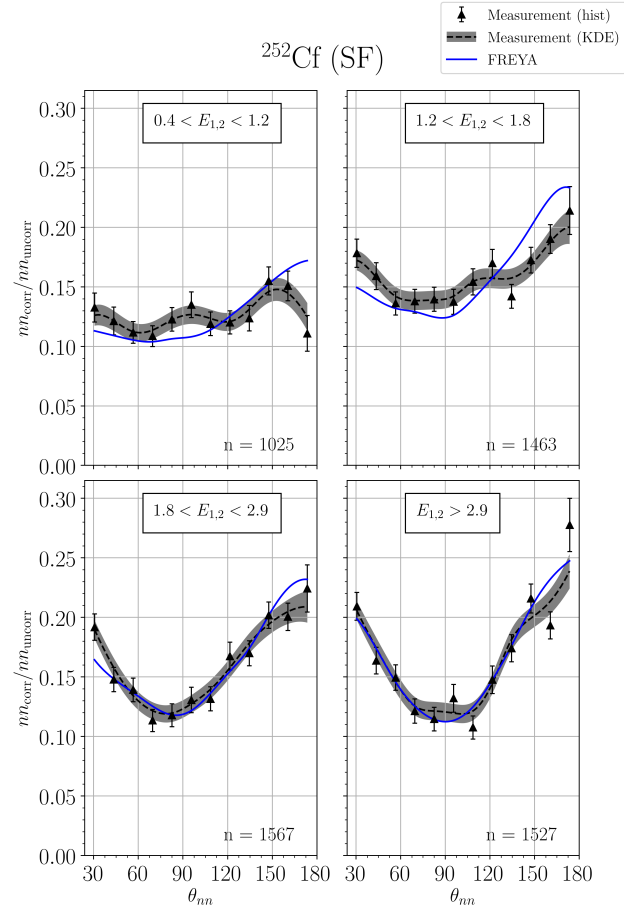


**FIG. 27:**  $\theta_{nn}$  distribution with cuts requiring that the energy of both coincident neutrons be within the specified range. The number of events contributing to each plot,  $n$ , is shown. Note that the lower right plots of this figure and Fig. 26 are identical.

987 fragment, because one neutron receives a boost to higher  
 988 energy from the fragment and the other a boost to lower  
 989 energy. The neutron boosted to lower energy is directed  
 990 toward the opposite fission fragment and is potentially  
 991 subject to interaction with it. On the other hand, Fig. 28  
 992 middle and bottom show no statistically significant de-  
 993 pendence in the correlation when maximum (middle) or  
 994 minimum (bottom) energy cuts are applied to each neu-  
 995 tron. To summarize the data, when both neutrons are  
 996 high energy and when both neutrons are low energy, there  
 997 does not seem to be an effect, but the effect is evident  
 998 when there is a difference in energy. This is suggestive  
 999 of a scenario whereby the decrease in correlation at large  
 1000 opening angles is associated with the emission of two neu-  
 1001 trons from the same fragment.

1002 A second possible explanation for this drop in n-n cor-  
 1003 relation at large opening angles is that there is, due to  
 1004 unknown reasons, a decrease in neutron emission along  
 1005 the fission axis. If it is the former case of shadowing, this  
 1006 effect has the potential to shed light on the time depen-

1007 dence of neutron emission, since shadowing would likely  
 1008 depend on the fission fragment separation. A definitive  
 1009 interpretation of this decreased n-n correlation for large  
 1010 opening angles in photofission requires further study.

### C. Considering $\theta_{abs}$

1012 As previously discussed in section IC, photofission dif-  
 1013 fers from spontaneous and neutron induced fission in that  
 1014 the fission fragments for the photon-induced reaction ex-  
 1015 hibit an asymmetry in their angle of emission, with the  
 1016 most likely orientation of the fission axis lying perpen-  
 1017 dicular to the direction of the incident photon. With  
 1018 this in mind, the following series of angular cuts were  
 1019 made on the data. Figure 29 shows the distributions of  
 1020 absolute angles of the n-n events for three different cuts  
 1021 on the value of the n-n opening angle. For n-n open-  
 1022 ing angles between  $120^\circ$  and  $160^\circ$ , there is an increased

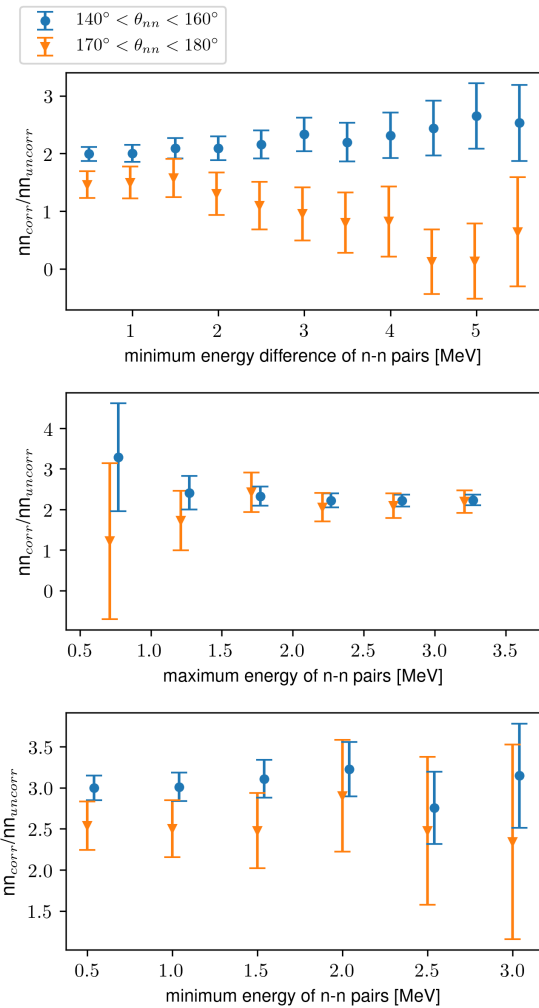


**FIG. 28:** From the photofission of  $^{238}\text{U}$ . The x-axes of each plot correspond to various cuts applied to the energies of the two neutrons forming coincident n-n pairs. (top) cuts are the minimum absolute difference between the energies of both coincident neutrons. (middle) cuts are a maximum energy threshold of both coincident neutrons, *i.e.* the left side of the plot corresponds to n-n pairs in which both neutrons have low energy. (bottom) cuts are a minimum energy threshold of both coincident neutrons, *i.e.* the right side of the plot corresponds to n-n pairs in which both neutrons have high energy.

1023 preponderance of both neutrons being emitted around  
1024  $90^\circ$ , consistent with the interpretation of kinematic fo-  
1025 cusing of neutrons coming from fission fragments which  
1026 are themselves being emitted preferentially at  $90^\circ$ . How-  
1027 ever, in the opening angle region where the n-n corre-  
1028 lation is reduced, from about  $160^\circ$  to  $180^\circ$ , this feature is  
1029 less prominent.

1030 Furthermore, if one plots the opening angle distribu-  
1031 tions for the case in which at least one neutron is emitted  
1032 perpendicular to the incident photon *versus* the case in  
1033 which neither neutron is emitted perpendicular to the  
1034 incident photon (Fig. 30), one sees distinct differences.

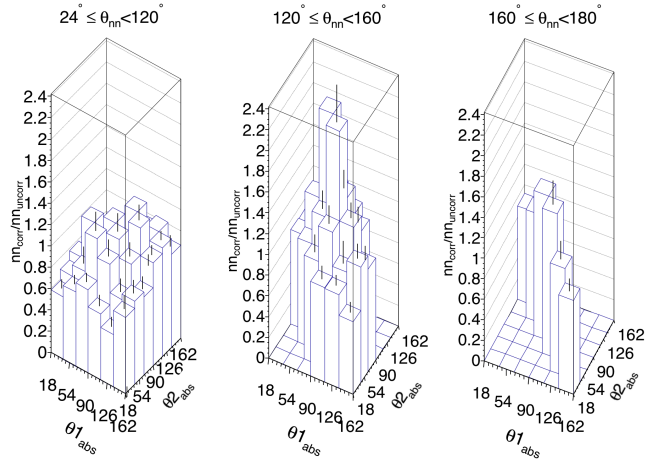


**FIG. 29:** Visualization of the correlation between the angles of each neutron with respect to the incident photon beam, denoted by  $\theta_{1\text{abs}}$  and  $\theta_{2\text{abs}}$ . Empty bins exist because of intrinsic geometrical phase-space. Data taken from measurements of  $^{238}\text{U}$  photofission.

1035 The fact that there are overall differences is not surpris-  
1036 ing, because in one case (Fig. 30 solid line) at least one  
1037 neutron preferentially receives a kinematic boost from a  
1038 fission fragment and in the other case (Fig. 30 dotted  
1039 line) neither neutron does. However, the fact that the  
1040 n-n correlation is reduced at  $180^\circ$  in opening angle when  
1041 at least one of the neutrons is emitted along the preferred  
1042 fission axis is unexpected. This is a feature which does  
1043 not seem to appear in most previous measurements of  
1044 either neutron-induced or spontaneous fission, as well as  
1045 our present measurement on spontaneous fission. The  
1046 attribution of this effect to the geometric coverage of the  
1047 neutron detection system or to neutron elastic scatter-  
1048 ing within the target was ruled out using simulations, as  
1049 discussed in section V C.

## 1050 VII. CONCLUDING REMARKS

1051 Neutron-neutron angular correlations in the photofis-  
1052 sion of  $^{238}\text{U}$  were measured using 10.5 MeV end-point  
1053 bremsstrahlung photons produced via a low duty factor,  
1054 pulsed linear electron accelerator. The measured angular  
1055 correlations reflect the underlying back-to-back nature of  
1056 the fission fragments. The method of analysis used a sin-  
1057 gle set of experimental data to produce an opening an-  
1058 gle distribution of correlated and uncorrelated neutron  
1059 pairs. A ratio is taken between these two sets to provide  
1060 a self-contained result of angular correlations, in that  
1061 the result is independent of neutron detector efficiencies.

1062 Neutron-neutron angular correlation measurements were  
1063 also made using neutrons from the spontaneous fission of  
1064  $^{252}\text{Cf}$  and show good agreement with previous measure-  
1065 ments.

1066 Measured n-n opening angle distributions from the  
1067 photofission of  $^{238}\text{U}$  are not in close agreement with the

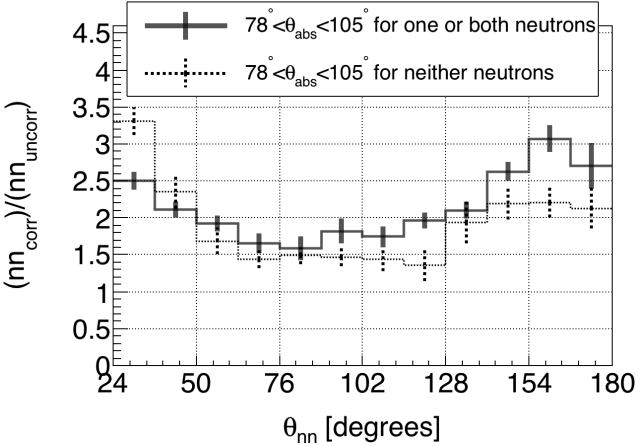


**FIG. 30:** Requiring that at least one of the coincident neutrons be emitted nearly perpendicular to the photon beam (solid line) produces an opening angle distribution that is different from that produced when it is required that both neutrons are emitted nearly parallel to the photon beam (dotted line). Data taken from measurements of  $^{238}\text{U}$  photofission.

ad hoc photofission model included in FREYA version 2.0.3. This is expected, because the model is only a crude approximation which uses a neutron-induced model to approximate photofission. The present measurement will be useful for fine-tuning photofission models included in future releases of FREYA.

In addition, we report for the first time a pronounced anomaly in the n-n angular distributions from photofission, in which the rate of neutron emission at opening angles near  $180^\circ$  is diminished, resulting in a local maximum at about  $160^\circ$  instead of the expected  $180^\circ$ . We offer two possible interpretations for this effect. First, the neutrons may indeed be emitted isotropically in the rest frame of the fission fragment, but one fragment essentially shadows the neutrons emitted from the other fragment, either through absorption or scattering. Second, that there is, due to unknown reasons, a decrease in neutron emission along the fission axis. While these measurements do not provide a definitive interpretation of this decreased n-n correlation for large opening angles in photofission, further study may have the potential to shed light on the time evolution of neutron emission in photofission.

It is our hope that these first measurements of n-n correlations in photofission will provide the impetus for future modeling of the fundamental physics of fission.

1094

## VIII. ACKNOWLEDGMENTS

This work has been supported by the National Nuclear Security Administration, grant DE-NA002488. We wish to thank the staff of the Idaho Accelerator Center for their assistance in this work. We also wish to acknowledge early contributions to this work by our friend and colleague the late David V. Jordan of the Pacific Northwest National Laboratory.

- 
- [1] J. T. Caldwell, E. J. Dowdy, R. A. Alvarez, B. L. Berman, and P. Meyer. Experimental determination of photofission neutron multiplicities for  $^{235}\text{U}$ ,  $^{236}\text{U}$ ,  $^{238}\text{U}$ , and  $^{232}\text{Th}$  using monoenergetic photons. *Nuclear Science and Engineering*, 73(2):153–163, 1980.
- [2] G. A. Petrov. Current status of the search for scission neutrons in fission and estimation of their main characteristics. *AIP Conference Proceedings*, 798(1):205–212, 2005.
- [3] Harry R. Bowman, Stanley G. Thompson, J. C. D. Milton, and Wladyslaw J. Swiatecki. Velocity and angular distributions of prompt neutrons from spontaneous fission of  $\text{Cf}^{252}$ . *Phys. Rev.*, 126:2120–2136, Jun 1962.
- [4] C. Budtz-Jørgensen and H.-H. Knitter. Simultaneous investigation of fission fragments and neutrons in  $^{252}\text{Cf}$  (SF). *Nuclear Physics A*, 490(2):307 – 328, 1988.
- [5] P. Talou, R. Vogt, J. Randrup, M. E. Rising, S. A. Pozzi, J. Verbeke, M. T. Andrews, S. D. Clarke, P. Jaffke, M. Jandel, T. Kawano, M. J. Marcath, K. Meierbachtol, L. Nakae, G. Rusev, A. Sood, I. Stetcu, and C. Walker. Correlated prompt fission data in transport simulations. *The European Physical Journal A*, 54(1):9, Jan 2018.
- [6] S. Debenedetti, J. E. Francis, W. M. Preston, and T. W. Bonner. Angular dependence of coincidences between fission neutrons. *Phys. Rev.*, 74:1645–1650, Dec 1948.
- [7] J. S. Pringle and F. D. Brooks. Angular correlation of neutrons from spontaneous fission of  $^{252}\text{Cf}$ . *Phys. Rev. Lett.*, 35:1563–1566, Dec 1975.
- [8] Sara A. Pozzi, Brian Wieger, Andreas Enqvist, Shaun D. Clarke, Marek Flaska, Matthew Marcath, Edward Larsen, Robert C. Haight, and Enrico Padovani. Correlated neutron emissions from  $^{252}\text{Cf}$ . *Nuclear Science and Engineering*, 178(2):250–260, 2014.
- [9] A. M. Gagarski, I. S. Guseva, V. E. Sokolov, G. V. Val'ski, G. A. Petrov, D. O. Krinitin, D. V. Nikolaev, T. A. Zavarukhina, and V. I. Petrova. Neutron-neutron angular correlations in spontaneous fission of  $^{252}\text{Cf}$ . *Bulletin of the Russian Academy of Sciences, Physics*, 72:773–777, July 2008.
- [10] J. M. Verbeke, L. F. Nakae, and R. Vogt. Neutron-neutron angular correlations in spontaneous fission of  $^{252}\text{Cf}$  and  $^{240}\text{Pu}$ . *Phys. Rev. C*, 97:044601, Apr 2018.
- [11] V. E. Sokolov and G. A. Petrov. Investigation of the angular dependences of neutron-neutron coincidences from  $^{252}\text{Cf}$ ,  $^{235}\text{U}$ ,  $^{233}\text{U}$  and  $^{239}\text{Pu}$  fission in search of scission neutrons. *Proc. XVIII Internat. Seminar on Interaction of Neutrons with Nuclei (ISSIN-18)*, pages 108–118, 2010.
- [12] Matthew J. Marcath, Tony H. Shin, Shaun D. Clarke, Paolo Peerani, and Sara A. Pozzi. Neutron angular distribution in plutonium-240 spontaneous fission. *Nuclear*

- 1152      *Instruments and Methods in Physics Research, Section 1172*  
 1153      *A: Accelerators, Spectrometers, Detectors and Associated 1173*  
 1154      *Equipment*, 830:163–169, 9 2016.  
 1155 [13] S Nair, D B Gayther, B H Patrick, and E M Bowey. 1174  
 1156      Fission-neutron and fragment angular distributions from 1176  
 1157      threshold photofission of  $^{232}\text{Th}$  and  $^{238}\text{U}$ . *Journal of 1177*  
 1158      *Physics G: Nuclear Physics*, 3(7):965, 1977.  
 1159 [14] J. M. Mueller, M. W. Ahmed, R. H. France, M. S. John- 1179  
 1160      son, H. J. Karwowski, L. S. Myers, J. Randrup, M. H. 1180  
 1161      Sikora, M. C. Spraker, S. Stave, J. R. Tompkins, R. Vogt, 1181  
 1162      H. R. Weller, C. S. Whisnant, and W. R. Zimmerman. 1182  
 1163      Prompt neutron polarization asymmetries in photofission 1183  
 1164      of  $^{232}\text{Th}$ ,  $^{233,235,238}\text{U}$ ,  $^{237}\text{Np}$ , and  $^{239,240}\text{Pu}$ . *Phys. Rev. 1184*  
 1165      *C*, 89:034615, Mar 2014.  
 1166 [15] Jefferson Lab. *CODA 2.6*, 2015.  
 1167 [16] Sara A Pozzi, Enrico Padovani, and Marzio Marseguerra. 1187  
 1168      MCNP-PoliMi: a Monte-Carlo code for correlation mea- 1188  
 1169      surements. *Nuclear Instruments and Methods in Physics 1189*  
 1170      *Research Section A: Accelerators, Spectrometers, Detec- 1190*  
 1171      *tors and Associated Equipment*, 513(3):550 – 558, 2003.  
 1191  
 1192 [17] Eric C. Miller, Shaun D. Clarke, Marek Flaska, Sara 1193  
 1194      A. Pozzi, and Enrico Padovani. MCNPX-PoliMi post-  
 1195      processing algorithm for detector response simulations. 1196  
 1196      *JNMM, Journal of the Institute of Nuclear Materials 1197*  
 1197      *Management*, 40(2):34–41, 12 2012.  
 1198 [18] Lawrence Berkeley National LaboratoryLawrence Liver-  
 1199      more National LaboratoryLos Almost National Labora-  
 1200      toryUniversity of Michigan Nuclear Engineering. *FREYA 2.0.3*, 2016.  
 1201 [19] S. D. Clarke, B. M. Wieger, A. Enqvist, R. Vogt, J. Ran-  
 1202      drup, R. C. Haight, H. Y. Lee, B. A. Perdue, E. Kwan,  
 1203      C. Y. Wu, R. A. Henderson, and S. A. Pozzi. Mea-  
 1204      surement of the energy and multiplicity distributions of  
 1205      neutrons from the photofission of  $^{235}\text{U}$ . *Phys. Rev. C*,  
 1206      95:064612, Jun 2017.  
 1207 [20] Krishichayan, M. Bhike, A. P. Tonchev, and W. Tornow.  
 1208      Fission product yield measurements using monoenergetic  
 1209      photon beams. In *European Physical Journal Web of 1210*  
 1210      *Conferences*, volume 146 of *European Physical Journal 1211*  
 1211      *Web of Conferences*, page 04018, September 2017.  
 1212 [21] Kyle Cranmer. Kernel estimation in high-energy physics.  
 1213      *Computer Physics Communications*, 136(3):198–207,  
 1214      2001.